

***d*-wave superfluidity in optical lattices of ultracold polar molecules**Kevin A. Kuns,¹ Ana Maria Rey,² and Alexey V. Gorshkov¹¹*Institute for Quantum Information, California Institute of Technology, Pasadena, California 91125, USA*²*JILA, National Institute of Standards and Technology and University of Colorado, Boulder, Colorado 80309-0440 and Department of Physics, University of Colorado, Boulder, Colorado 80309-0390, USA*

(Received 24 October 2011; published 29 December 2011)

Recent work on ultracold polar molecules, governed by a generalization of the t - J Hamiltonian, suggests that molecules may be better suited than atoms for studying d -wave superfluidity due to stronger interactions and larger tunability of the system. We compute the phase diagram for polar molecules in a checkerboard lattice consisting of weakly coupled square plaquettes. In the simplest experimentally realizable case where there is only tunneling and an XX -type spin-spin interaction, we identify the parameter regime where d -wave superfluidity occurs. We also find that the inclusion of a density-density interaction destroys the superfluid phase and that the inclusion of a spin-density or an Ising-type spin-spin interaction can enhance the superfluid phase. We also propose schemes for experimentally realizing the perturbative calculations exhibiting enhanced d -wave superfluidity.

DOI: [10.1103/PhysRevA.84.063639](https://doi.org/10.1103/PhysRevA.84.063639)

PACS number(s): 67.85.-d, 71.10.Fd, 74.20.Mn, 74.20.Rp

I. INTRODUCTION

The Hubbard Hamiltonian is believed to contain some of the ingredients necessary to explain high-temperature superconductivity in cuprates [1–3]. The difficulties of analytically understanding the Hubbard Hamiltonian in more than one dimension suggest the use of experimental quantum simulators to investigate the physics of this model, and important experimental progress in this direction has been made with lattices of ultracold atoms [4–10]. In the context of high-temperature superconductivity, the most relevant regime of the Hubbard Hamiltonian is the limit of strong on-site interactions, in which the model reduces to the t - J Hamiltonian [1–3]. Here t is the nearest-neighbor tunneling amplitude and J is the nearest-neighbor exchange interaction originating from second-order virtual hopping. Unfortunately, the exchange interactions are so small that it is extremely difficult to observe the associated physics in the cold-atom implementation [8].

Recently, the polar molecules KRb and LiCs have been cooled to their electronic, rotational, and vibrational ground states [11–14], and KRb has been loaded into a three-dimensional optical lattice [15]. This system can be used to implement lattice Hamiltonians based on rotational states of polar molecules [16–32]. Specifically, two rotational states of the molecules can be used as an effective spin-1/2 degree of freedom, while dipole-dipole interactions mediate “spin”-dependent coupling between molecules. For molecules on neighboring sites, the strength of these dipole-dipole interactions is ~ 1 kHz for KRb and ~ 100 kHz for LiCs. These interactions are much stronger than the exchange interactions between ultracold atoms ($\ll 1$ kHz [9]). Therefore, polar molecules seem to be better candidates for the simulation of certain condensed matter phenomena.

Recently, it was shown that polar molecules in optical lattices can be used to simulate a highly tunable generalization of the t - J Hamiltonian, referred to as the t - J - V - W Hamiltonian [30,31]. The latter differs from the t - J Hamiltonian in the following aspects: it has anisotropic XXZ spin-spin interactions J_{\perp} and J_z , an independent density-density interaction V , a spin-density interaction W , and the interactions are long-range dipolar rather than nearest-neighbor. This

Hamiltonian is highly tunable, and the strengths of these interactions can, in principle, be varied independently in experiments. In particular, the regime $J > t$ can be achieved, which is not possible with cold atoms where J originates from second-order virtual hopping. Furthermore, in Ref. [31], it was shown that, in one dimension, the t - J - V - W model can support enhanced superfluidity relative to the standard t - J model.

In this paper, we use the tunability of the t - J - V - W Hamiltonian to find parameter regimes supporting robust d -wave superfluidity in one- and two-dimensional systems of weakly coupled plaquettes [33–38]. Furthermore, we demonstrate that this solvable limit and the associated d -wave superfluidity are experimentally realizable. Finally, we believe that this limit can provide qualitative guidance for the case of the homogeneous two-dimensional lattice.

Throughout the paper, we consider, for simplicity, an average filling of three molecules per plaquette. In the simplest experimentally realizable case where $J_z = V = W = 0$, referred to as the t - J_{\perp} Hamiltonian, we find three phases: a d -wave superfluid of bound holes, a checkerboard solid of alternating plaquettes of bound holes, and phase separation of bound holes. We find that the addition of a density-density interaction proportional to V destroys the superfluid phase in the perturbative limit. We also find that an Ising-type spin-spin interaction proportional to J_z or a spin-density interaction proportional to W can enhance the superfluid phase for certain parameter regimes.

The remainder of the paper is organized as follows. In Sec. II, we introduce the t - J - V - W Hamiltonian and briefly discuss its experimental implementation with polar molecules in optical lattices. In Sec. III, we analyze the t - J_{\perp} Hamiltonian in detail solving the single-plaquette Hamiltonian exactly and calculating the phase diagram perturbatively. In Sec. IV, we analyze the effects of the J_z , V , and W terms on the superfluid phase. In Sec. V, we present proposals for experimentally realizing the perturbative calculations for one- and two-dimensional systems of plaquettes. Finally, in Sec. VI, we present conclusions. Appendix A gives a brief summary of the group theoretic techniques used to solve the single-plaquette Hamiltonians exactly and describes the symmetries

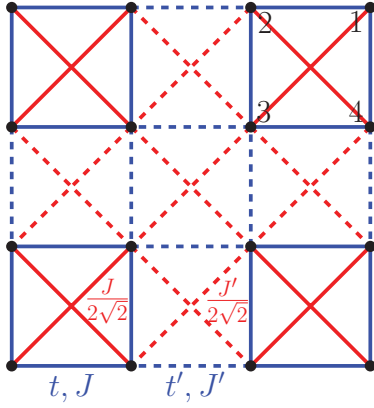


FIG. 1. (Color online) Geometry of plaquettes. J schematically denotes all dipolar interactions J_{\perp} , J_z , V , and W . Within each plaquette, solid blue lines contain tunneling of amplitude t and dipolar interactions of strength J , while solid red lines only contain dipolar interactions of strength $J/(2\sqrt{2})$. Nearest-neighbor plaquettes are then linked with tunneling of amplitude t' and dipolar interactions of strength J' , shown as dotted blue lines, where $t' \ll t$ and $J' \ll J$. Furthermore, nearest-neighbor and next-nearest-neighbor plaquettes are linked with dipolar interactions of strength $J'/(2\sqrt{2})$, shown as dotted red lines. The numbering of sites in a single plaquette is shown in black.

of the solutions. Appendix B gives explicit expressions for the basis vectors of the irreducible representations discussed in Appendix A, and Appendix C gives explicit expressions for important ground-state energies and states.

II. THE t - J - V - W HAMILTONIAN

In the following calculations, we consider nearest-neighbor and next-nearest-neighbor interactions on a square lattice as shown in Fig. 1 and approximate the Hamiltonian [30,31] as

$$\begin{aligned}
 H = & - \sum_{\langle r,r' \rangle, \sigma} t_{rr'} (c_{r\sigma}^{\dagger} c_{r'\sigma} + c_{r'\sigma}^{\dagger} c_{r\sigma}) \\
 & + \left(\sum_{\langle r,r' \rangle} + \frac{1}{2\sqrt{2}} \sum_{\langle\langle r,r' \rangle\rangle} \right) \left[\frac{J_{\perp rr'}}{2} (S_r^+ S_{r'}^- + S_r^- S_{r'}^+) \right. \\
 & \left. + J_{zrr'} S_r^z S_{r'}^z + V_{rr'} n_r n_{r'} + W_{rr'} (n_r S_{r'}^z + n_{r'} S_r^z) \right], \quad (1)
 \end{aligned}$$

where $c_{r\sigma}^{\dagger}$ is the creation operator for a hardcore fermionic molecule at the lattice site r with effective spin σ , $n_{r\sigma} = c_{r\sigma}^{\dagger} c_{r\sigma}$, $n_r = n_{r\uparrow} + n_{r\downarrow}$, $S_r^+ = c_{r\uparrow}^{\dagger} c_{r\downarrow}$, $S_r^- = (S_r^+)^{\dagger}$, and $S_r^z = (n_{r\uparrow} - n_{r\downarrow})/2$. The tunneling amplitude $t_{rr'}$ and the dipolar interaction strengths $J_{\perp rr'}$, $J_{zrr'}$, $V_{rr'}$, and $W_{rr'}$ are t , J_{\perp} , J_z , V , and W , respectively, if the sites r and r' are in the same plaquette and are t' , J'_{\perp} , J'_z , V' , and W' , respectively, if the sites are in neighboring plaquettes. The $\langle \rangle$ signify that the sums are taken over nearest-neighbor bonds and the $\langle\langle \rangle\rangle$ signify that the sums are taken over next-nearest-neighbor (diagonal) bonds. The next-nearest-neighbor bonds have a factor of $1/(2\sqrt{2})$ since they are a factor of $\sqrt{2}$ longer than the nearest-neighbor bonds and since the dipole-dipole interaction strength falls off inversely as distance cubed. Equation (1) omits the energies

of the states $|\uparrow\rangle$ and $|\downarrow\rangle$ since we work at fixed numbers of up and down molecules.

The Hamiltonian given by Eq. (1) could be experimentally realized by loading ultracold polar molecules into an optical lattice and applying an external dc electric field perpendicular to the plane of the lattice [30,31]. Two rotational states $|m_0\rangle$ and $|m_1\rangle$ of a molecule form the effective spin states $|\uparrow\rangle$ and $|\downarrow\rangle$, respectively. The preparation of these states is discussed below in Sec. VA 2. Due to the dc electric field, these states have permanent electric dipole moments. The J_z , V , and W interaction terms in Eq. (1) can be understood as the classical dipole-dipole interactions between these permanent dipole moments. The J_{\perp} interaction term arises due to the transition dipole moment between $|m_0\rangle$ and $|m_1\rangle$. Large chemical reaction rates [39–41] and large interactions between molecules on the same lattice site enforce the hardcore constraint [30].

The amplitudes and signs of J_{\perp} , J_z , V , and W can be tuned independently [30] by tuning the external dc electric field and applying external microwave fields [17–19,21–25,29,42–46]. The tunneling amplitude t (assumed to be positive throughout the paper) can be tuned by adjusting the depth of the optical lattice.

III. ANALYSIS OF THE t - J_{\perp} HAMILTONIAN

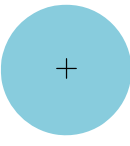
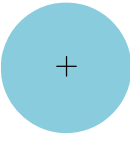
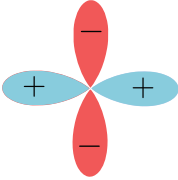
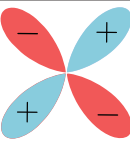
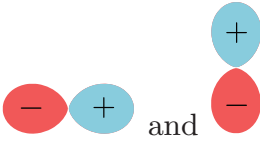
The simplest experimental realization of Eq. (1) can be obtained by applying a very weak external dc electric field. In this case, the permanent electric dipole moments are very small, making J_z , V , and W negligible relative to J_{\perp} , which is proportional to the square of the transition dipole moment. In this section, we study the resulting t - J_{\perp} Hamiltonian given by Eq. (1) with $J_z = V = W = 0$ and $J'_z = V' = W' = 0$. In Sec. III A, we describe the exact diagonalization of the t - J_{\perp} Hamiltonian for a single plaquette and identify a set of conditions necessary, within our perturbative analysis, for the observation of d -wave superfluidity. In Sec. III B, we calculate the phase diagram for a two-dimensional lattice of plaquettes perturbatively.

Throughout the remainder of this paper, we use the following notation for states. A ket with one number $|n\rangle$ refers to a single plaquette with $n = n_{\uparrow} + n_{\downarrow}$ total molecules. A ket with two numbers separated by a comma $|n_{\uparrow}, n_{\downarrow}\rangle$ refers to a single plaquette with n_{\uparrow} spin-up molecules and n_{\downarrow} spin-down molecules. A tensor product of two kets $|n_R\rangle |n_{R'}\rangle$ refers to a system of two plaquettes with n_R total molecules on plaquette R and $n_{R'}$ total molecules on plaquette R' .

A. Single-plaquette analysis

We use the point symmetries of the square, described by the group D_4 , and the conservation laws of the Hamiltonian to simplify the task of diagonalizing the single-plaquette Hamiltonian with Hilbert space dimension $3^4 = 81$ and to understand the symmetries of the resulting eigenstates. First, the operators n_{\uparrow} and n_{\downarrow} (which measure the number of up and down molecules on a single plaquette) commute with the Hamiltonian and with each other, so we can diagonalize subspaces with fixed values of n_{\uparrow} and n_{\downarrow} separately. This reduces the subspace dimensions to 12 for the largest subspaces. We

TABLE I. (Color online) Symmetries corresponding to the irreducible representations of the group D_4 as is discussed in Appendix A [33,38,47]. Wave-function symmetries are plotted in the x - y plane. Note that the A_1 representation is symmetric under all symmetry operations of the square and that the A_2 representation is antisymmetric under π rotations about the x and y axes and the lines $y = x$ and $y = -x$. The A_2 wave functions can be thought of as being positive (blue) on the front and negative (red) on the back, while all other wave functions have the same polarity on both sides of the wave function.

Representation	Symmetries	
A_1	s	
A_2	s	
B_1	$d_{x^2-y^2}$	
B_2	d_{xy}	
E	p_x and p_y	

then use the basis functions of the group D_4 to diagonalize the Hamiltonian for each irreducible representation separately. This requires diagonalizing 3×3 matrices at worst. The symmetries of the resulting eigenstates correspond to the symmetries of the irreducible representations summarized in Table I.

The Hamiltonians for subspaces of constant n_\uparrow and n_\downarrow were diagonalized in the representation basis using the methods described below in Appendix A. The ground states of a single plaquette with fixed total number of molecules $n = n_\uparrow + n_\downarrow$ are summarized in Table II. In order to construct robust *d*-wave superfluids at 3/4 filling (three molecules per plaquette), we would like it to be energetically favorable for two holes to condense on the same plaquette. This condition is achieved if the binding energy of two holes [33–38]

$$\Delta_t = 2E_g(3) - E_g(4) - E_g(2) \quad (2)$$

is positive, where $E_g(n)$ is the energy of the ground state of $|n\rangle$. Δ_t is shown in Fig. 2(a). The *d*-wave matrix element between

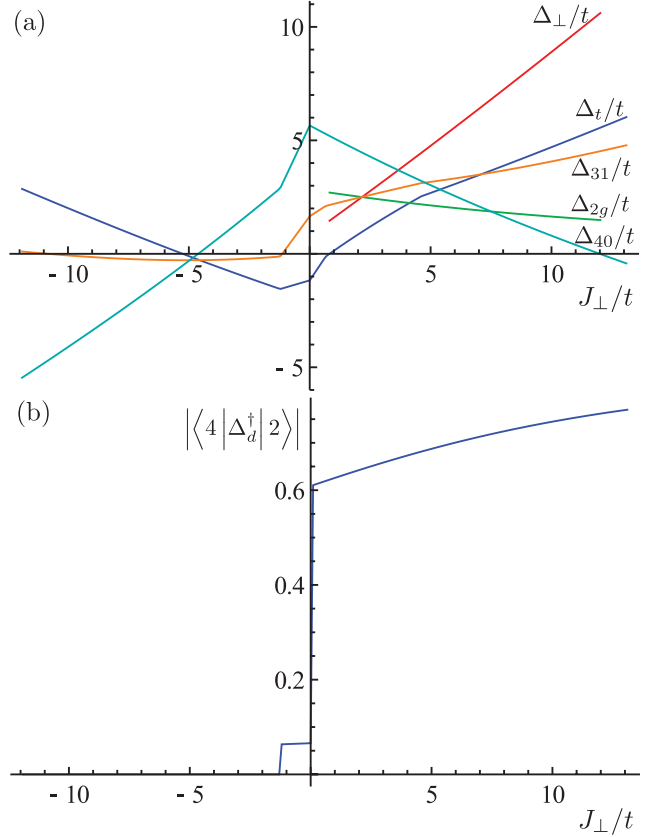


FIG. 2. (Color online) (a) Binding energy Δ_t for two holes and other relevant energies Δ_\perp , Δ_{31} , Δ_{40} , and Δ_{2g} , all of which must be positive for the Hamiltonian to support *d*-wave superfluidity within our treatment. (b) $|\langle 4 | \Delta_d^\dagger | 2 \rangle|$ for a single plaquette, which must be nonzero for the Hamiltonian to support *d*-wave superfluidity within our treatment.

$|2\rangle$ and $|4\rangle$

$$\langle 4 | \Delta_d^\dagger | 2 \rangle$$

must also be nonzero for *d*-wave superfluidity to be possible. Δ_d^\dagger is the *d*-wave symmetric pair creation operator defined as [37,48]

$$\Delta_d^\dagger = \frac{1}{2}(s_{12}^\dagger + s_{34}^\dagger - s_{14}^\dagger - s_{23}^\dagger), \quad (3)$$

where

$$s_{rr'}^\dagger = \frac{1}{\sqrt{2}}(c_{r\uparrow}^\dagger c_{r'\downarrow}^\dagger - c_{r\downarrow}^\dagger c_{r'\uparrow}^\dagger) \quad (4)$$

creates a singlet between sites r and r' . Since $s_{rr'}^\dagger = s_{r'r}^\dagger$, Δ_d^\dagger has $d_{x^2-y^2}$ symmetry and creates a pair of molecules with $d_{x^2-y^2}$ symmetry. Thus, the condition $\langle 4 | \Delta_d^\dagger | 2 \rangle \neq 0$ ensures *d*-wave symmetry of bound hole pairs. $|\langle 4 | \Delta_d^\dagger | 2 \rangle|$ is shown in Fig. 2(b).

From the information in Table II, we can understand the behavior of Δ_t and $|\langle 4 | \Delta_d^\dagger | 2 \rangle|$ shown in Fig. 2. We see that for all values of J_\perp/t , the ground state of $|4\rangle$ is a $|2,2\rangle$ in the B_1 representation and thus always has $d_{x^2-y^2}$ symmetry. For $J_\perp/t < -1.22$, the ground state of $|2\rangle$ is a $|1,1\rangle$ in the E representation and thus cannot exhibit *d*-wave superfluidity.

TABLE II. Ground-state configurations and symmetries of states with constant $n = n_\uparrow + n_\downarrow$. The results are symmetric under interchange of up spins with down spins. The ground state for four molecules is always $|2,2\rangle$ in the B_1 representation; however, there are two copies of the B_1 representation for the $|2,2\rangle$ subspace, see Appendix A, and the particular ground state changes at $J_\perp/t = 0$ even though the symmetry of the ground state remains $d_{x^2-y^2}$.

J_\perp/t	n_\uparrow, n_\downarrow	Representation
$\in(-\infty, \infty)$	1,0	A_1
< -1.22	1,1	E
> -1.22	1,1	A_1
< 0	2,1	A_2
$\in(0, 0.66)$	3,0	A_2
$\in(0.66, 4.62)$	2,1	E
> 4.62	2,1	B_1
< 0	2,2	B_1
> 0	2,2	B_1

For $J_\perp/t > -1.22$, the ground state changes to a $|1,1\rangle$ in the A_1 representation and thus has s -wave symmetry. This change in representations accounts for $|\langle 4|\Delta_d^\dagger|2\rangle|$ becoming nonzero at $J_\perp/t = -1.22$ and the kink in Δ_t at the same value. The change in the $|4\rangle$ ground state at $J_\perp/t = 0$, while retaining the $d_{x^2-y^2}$ symmetry, accounts for the large jump in $|\langle 4|\Delta_d^\dagger|2\rangle|$ at this value.

For $0 < J_\perp/t < 0.66$, the ground states of $|3\rangle$ are a $|3,0\rangle$ and a $|0,3\rangle$ in the A_2 representation; for all other values of J_\perp/t , the ground states are a $|2,1\rangle$ and a $|1,2\rangle$. At $J_\perp/t = 0.66$, the state changes to the E representation and at $J_\perp/t = 4.62$ the state changes to the B_1 representation. These changes in representations account for the kinks in Δ_t at these values of J_\perp/t . Δ_t crosses the positive J_\perp/t axis at $J_\perp/t = 0.82$. For $J_\perp/t > 0.82$, the condition $|\langle 4|\Delta_d^\dagger|2\rangle| \neq 0$ also holds. Thus in this regime, holes bind into d -wave symmetric pairs, which are necessary for d -wave superfluidity.

The t - J_\perp Hamiltonian is an improvement over the Hubbard Hamiltonian in that the binding energy Δ_t for the Hubbard Hamiltonian is positive only for a narrow parameter region $0 < U/t < 4.6$ [37]. Furthermore, the binding energy reaches a maximum for the Hubbard Hamiltonian [37] while it increases with J_\perp/t for the t - J_\perp Hamiltonian.

For positive values, the binding energy Δ_t is the amount that the ground state $|2\rangle|4\rangle$ or $|4\rangle|2\rangle$ is energetically favorable over the ground state $|3\rangle|3\rangle$, which could be coupled to $|2\rangle|4\rangle$ and $|4\rangle|2\rangle$ through tunneling t' . For positive values of Δ_t it is also necessary to consider the energy difference between the lowest energy states coupled to $|2\rangle|4\rangle$ and $|4\rangle|2\rangle$ through the spin interaction J'_\perp :

$$\Delta_\perp = E_g(0,2) + E_g(3,1) - E_g(1,1) - E_g(2,2),$$

where $E_g(n_\uparrow, n_\downarrow)$ is the energy of the lowest $|n_\uparrow, n_\downarrow\rangle$ state. Δ_\perp is shown in Fig. 2(a) for values of J_\perp/t where $\Delta_t > 0$ and $|\langle 4|\Delta_d^\dagger|2\rangle| \neq 0$. The sizes of the binding energies Δ_t and Δ_\perp

roughly correspond to how large t' and J'_\perp can be, respectively, to stay within the perturbative limit.

For $J_\perp/t > -1.22$, the ground state of $|2\rangle$ is an s -wave $|1,1\rangle$ in the A_1 representation. However, another $|1,1\rangle$ state in the E representation becomes close in energy to the ground state for large J_\perp/t . So we define a third energy difference

$$\Delta_{2g} = E_g(1,1(E)) - E_g(1,1(A_1))$$

to quantify the energy gap between these two $|2\rangle$ states. Here $E_g(1,1(\Gamma))$ is the energy of the lowest $|1,1\rangle$ state in the irreducible representation Γ . Δ_{2g} roughly corresponds to how large the overall perturbing Hamiltonian H_{eff} linking plaquettes can be to stay within the region of validity of our analysis. Δ_{2g} is also shown in Fig. 2(a) for values of J_\perp/t , where $\Delta_t > 0$ and $\langle 4|\Delta_d^\dagger|2\rangle \neq 0$.

Provided that $\Delta_t > 0$, in a full lattice of decoupled plaquettes with $3/8$ of the lattice sites occupied by up molecules and $3/8$ of the lattice sites occupied by down molecules, it could, in principle, be energetically favorable for the molecules to arrange themselves in configurations other than two and four molecules on a plaquette throughout the entire lattice. Since $\Delta_t > 0$, it will be energetically costly to change $|2\rangle|4\rangle$ to $|3\rangle|3\rangle$. Two four-molecule plaquettes $|4\rangle|4\rangle$ cannot rearrange their molecules since they are at maximum filling. However, it is possible for two two-molecule plaquettes $|2\rangle|2\rangle$ to rearrange themselves to $|3\rangle|1\rangle$ or $|4\rangle|0\rangle$. Thus, it is also necessary to consider the binding energies

$$\Delta_{31} = E_g(3) + E_g(1) - 2E_g(2)$$

and

$$\Delta_{40} = E_g(4) + E_g(0) - 2E_g(2) = E_g(4) - 2E_g(2).$$

Both Δ_{31} and Δ_{40} are shown in Fig. 2(a).

As is shown in Fig. 2(a), when Δ_t is positive, the other relevant energies are also positive for J_\perp/t less than about 12. For J_\perp/t greater than about 12, Δ_{40} becomes negative, and it becomes energetically favorable for a $|2\rangle|2\rangle$ to change to a $|4\rangle|0\rangle$ or $|0\rangle|4\rangle$, in which case the manifold of states consisting of only $|2\rangle$ and $|4\rangle$ plaquettes stops being the true ground state. However, the phase diagram based on $|2\rangle$ and $|4\rangle$ plaquettes can still be studied experimentally by adiabatically preparing these (no longer ground) states beginning with easily preparable excited states. A calculation to minimize the energy of a full lattice of plaquettes with $t' = J'_\perp = 0$ confirms that a lattice with half of the plaquettes as $|2\rangle$ and half as $|4\rangle$ is the ground state when Δ_{40} and Δ_t are positive.

Although it is outside the scope of the present paper, we point out that the narrow region $0 < J_\perp/t < 0.66$, where $|0,3\rangle$ and $|3,0\rangle$ are the degenerate ground states, could support Nagaoka ferromagnetism [49,50].

B. Double-plaquette analysis

In this section, we describe the behavior of the full lattice of plaquettes. We use Schrieffer-Wolff transformations to find the interactions between nearest-neighbor and next-nearest-neighbor plaquettes to second order in t'/t and J'_\perp/t . We then derive an effective XXZ Hamiltonian and solve for the phase diagram in the perturbative limit.

1. Schrieffer-Wolff transformations

We solve the problem of two coupled plaquettes with second-order perturbation theory through the Schrieffer-Wolff transformation [51]. There are six relevant double-plaquette problems in describing a full two-dimensional lattice. A $|4\rangle$ can interact with another $|4\rangle$ or with a $|2\rangle$, and a $|2\rangle$ can also interact with another $|2\rangle$. For each of these three cases, the plaquettes can be situated either next to each other or diagonally.

In all cases, the unperturbed Hamiltonian is the tensor product of two single-plaquette Hamiltonians

$$H_0 = \begin{bmatrix} 0 & 0 \\ 0 & U \end{bmatrix} \quad (5)$$

written here in the basis that diagonalizes it. If the dimension of the two-plaquette Hilbert space is d and the ground state is l -fold degenerate, then the upper left 0 is an $l \times l$ zero matrix and U is a $(d - l) \times (d - l)$ diagonal matrix with the energy differences between the ground and excited states along the diagonal. The $|2\rangle$ and $|4\rangle$ energies differ; however, since the number of $|2\rangle$ and $|4\rangle$ plaquettes is constant, we drop these energies here.

The perturbing Hamiltonian is

$$H_1 = \begin{bmatrix} H_{1g} & H_{1ge} \\ H_{1ge}^T & H_{1e} \end{bmatrix},$$

where H_{1g} defines the first-order shifts in the energies of the ground states due to the perturbation, H_{1ge} defines the couplings between the ground and excited states, and H_{1e} defines the couplings between the excited states and the first-order shifts in the energies of the excited states. The effective Hamiltonian for the low-energy subspace is then

$$H_{\text{eff}} = H_{1g} - H_{1ge}U^{-1}H_{1ge}^T + \dots \quad (6)$$

For the remainder of the paper, we divide the Hamiltonians by t . The first term then is of order t'/t and J'_\perp/t , while the second term is of order $(t'/t)^2$ and $(J'_\perp/t)^2$.

We then have the following effective Hamiltonians when the two plaquettes are situated next to each other:

$$H_{\text{eff}}^{(4,2)} = \begin{bmatrix} f^{(4,2)} & g^{(4,2)} \\ g^{(4,2)} & f^{(4,2)} \end{bmatrix} \text{ basis } \begin{bmatrix} |2\rangle|4\rangle \\ |4\rangle|2\rangle \end{bmatrix}, \quad (7a)$$

$$H_{\text{eff}}^{(2,2)} = f^{(2,2)} \text{ basis } |2\rangle|2\rangle, \quad (7b)$$

$$H_{\text{eff}}^{(4,4)} = f^{(4,4)} \text{ basis } |4\rangle|4\rangle, \quad (7c)$$

where

$$f^{(4,2)} = \left(\frac{t'}{t}\right)^2 f_t^{(4,2)} \left(\frac{J_\perp}{t}\right) + \left(\frac{J'_\perp}{t}\right)^2 f_\perp^{(4,2)} \left(\frac{J_\perp}{t}\right), \quad (8a)$$

$$g^{(4,2)} = \left(\frac{t'}{t}\right)^2 g_t^{(4,2)} \left(\frac{J_\perp}{t}\right), \quad (8b)$$

$$f^{(2,2)} = \left(\frac{t'}{t}\right)^2 f_t^{(2,2)} \left(\frac{J_\perp}{t}\right) + \left(\frac{J'_\perp}{t}\right)^2 f_\perp^{(2,2)} \left(\frac{J_\perp}{t}\right), \quad (8c)$$

$$f^{(4,4)} = \left(\frac{J'_\perp}{t}\right)^2 f_\perp^{(4,4)} \left(\frac{J_\perp}{t}\right). \quad (8d)$$

Here the functions f and g on the right-hand sides depend on the interaction strength J_\perp/t and describe the perturbative

coupling of the plaquettes. The superscript $(n_R, n_{R'})$ refers to the number of molecules on neighboring plaquettes R and R' . The subscripts t and \perp refer to interplaquette couplings driven by t' and J'_\perp , respectively. For the t - J_\perp Hamiltonian, there are no first-order shifts in the ground-state energies so there are no terms proportional to J'_\perp/t . The $|2\rangle|4\rangle$ and $|4\rangle|2\rangle$ states are only coupled through tunneling to second order, so there is no $g_\perp^{(4,2)}$ function. The $|4\rangle|4\rangle$ state cannot couple to itself through tunneling since both plaquettes are fully occupied, so there is no $f_t^{(4,4)}$ function.

The effective Hamiltonians for two plaquettes situated diagonally are

$$H_{\text{eff}}^{(4,2)} = \begin{bmatrix} h^{(4,2)} & 0 \\ 0 & h^{(4,2)} \end{bmatrix} \text{ basis } \begin{bmatrix} |2\rangle|4\rangle \\ |4\rangle|2\rangle \end{bmatrix}, \quad (9a)$$

$$H_{\text{eff}}^{(2,2)} = h^{(2,2)} \text{ basis } |2\rangle|2\rangle, \quad (9b)$$

$$H_{\text{eff}}^{(4,4)} = h^{(4,4)} \text{ basis } |4\rangle|4\rangle, \quad (9c)$$

where

$$h^{(4,2)} = \left(\frac{J'_\perp}{t}\right)^2 h_\perp^{(4,2)} \left(\frac{J_\perp}{t}\right), \quad (10a)$$

$$h^{(2,2)} = \left(\frac{J'_\perp}{t}\right)^2 h_\perp^{(2,2)} \left(\frac{J_\perp}{t}\right), \quad (10b)$$

$$h^{(4,4)} = \left(\frac{J'_\perp}{t}\right)^2 h_\perp^{(4,4)} \left(\frac{J_\perp}{t}\right). \quad (10c)$$

When the plaquettes are situated diagonally, there is no tunneling between them, so there are no terms proportional to $(t'/t)^2$. In particular, the $|2\rangle|4\rangle$ and $|4\rangle|2\rangle$ states cannot couple to each other through tunneling to second order, so the off-diagonal terms are zero.

2. XXZ Effective Hamiltonian

The full lattice of plaquettes can be mapped to an XXZ spin Hamiltonian [33,35,37,38] where each plaquette becomes a lattice site, labeled by R , and the states $|2\rangle$ and $|4\rangle$ of two and four molecules become the effective spin-up $|\uparrow\rangle$ and spin-down $|\downarrow\rangle$ states, respectively. Using the functions Eqs. (8) and Eqs. (10) calculated using the Schrieffer-Wolff transformation, the effective Hamiltonian is

$$H_{\text{eff}} = \sum_{\langle R, R' \rangle} [f^{(4,2)}(n_{R\uparrow}n_{R'\downarrow} + n_{R\downarrow}n_{R'\uparrow}) + g^{(4,2)}(S_R^+ S_{R'}^- + S_R^- S_{R'}^+) + f^{(2,2)}n_{R\uparrow}n_{R'\uparrow} + f^{(4,4)}n_{R\downarrow}n_{R'\downarrow}] + \sum_{\langle\langle R, R' \rangle\rangle} [h^{(4,2)}(n_{R\uparrow}n_{R'\downarrow} + n_{R\downarrow}n_{R'\uparrow}) + h^{(2,2)}n_{R\uparrow}n_{R'\uparrow} + h^{(4,4)}n_{R\downarrow}n_{R'\downarrow}].$$

Since each site R has either one spin-up or one spin-down,

$$n_{R\uparrow} = \frac{1}{2} + S_R^Z \quad \text{and} \quad n_{R\downarrow} = \frac{1}{2} - S_R^Z.$$

Thus, dropping constant terms,

$$H_{\text{eff}} = \sum_{\langle R, R' \rangle} [\tilde{J}_\perp (S_R^X S_{R'}^X + S_R^Y S_{R'}^Y) + \tilde{J}_{z1} S_R^Z S_{R'}^Z] + \sum_{\langle\langle R, R' \rangle\rangle} \tilde{J}_{z2} S_R^Z S_{R'}^Z + \tilde{B} \sum_R S_R^Z, \quad (11)$$

where

$$\tilde{J}_\perp = 2g^{(4,2)}, \quad (12a)$$

$$\tilde{J}_{z1} = f^{(2,2)} + f^{(4,4)} - 2f^{(4,2)}, \quad (12b)$$

$$\tilde{J}_{z2} = h^{(2,2)} + h^{(4,4)} - 2h^{(4,2)}, \quad (12c)$$

$$\tilde{B} = 2(f^{(2,2)} - f^{(4,4)} + h^{(2,2)} - h^{(4,4)}). \quad (12d)$$

Since we are interested in the phase diagram at constant $3/4$ filling of the lattice with molecules, $\sum_R S_R^Z = 0$ is constant in the XXZ effective Hamiltonian, so we can neglect the magnetic field term \tilde{B} . In fact, for the same reason, we have already dropped the energies of $|2\rangle$ and $|4\rangle$ in H_0 [Eq. (5)].

3. Phase diagram for the t - J_\perp Hamiltonian

If we only consider nearest-neighbor interactions between plaquettes, then $\tilde{J}_{z2} = 0$. In this case, there are three phases, which can be qualitatively understood by considering the following limits of the XXZ model [52]. If $\tilde{J}_{z1} \gg |\tilde{J}_\perp|$, it is energetically favorable for the spins to be antiferromagnetically ordered in the Z direction corresponding to a checkerboard solid of bound holes. If $\tilde{J}_{z1} \ll -|\tilde{J}_\perp|$, it is energetically favorable for the spins to be ferromagnetically ordered in the Z direction; however, since $\sum_R S_R^Z$ is fixed, this corresponds to a phase separation of the spins and a phase separation of the bound holes. Finally, if $|\tilde{J}_\perp| \gg |\tilde{J}_{z1}|$, it is energetically favorable for the spins to be ordered in the XY plane, which corresponds to a superfluid of bound holes. Specifically, for $\tilde{J}_\perp < 0$ ($\tilde{J}_\perp > 0$), the spin order is ferromagnetic (antiferromagnetic), corresponding to a d -wave superfluid with correlation function $\langle \Delta_{d,R}^\dagger \Delta_{d,R'} \rangle$ whose sign has uniform (checkerboard) structure in the R - R' plane. Since \tilde{J}_\perp can be mapped to $-\tilde{J}_\perp$ by a sublattice rotation [52], we do not distinguish, for $|\tilde{J}_\perp| \gg |\tilde{J}_{z1}|$, between the ferromagnetic and antiferromagnetic cases and simply refer to both phases as a d -wave superfluid. The phase transitions occur at $|\tilde{J}_\perp| = |\tilde{J}_{z1}|$ [52,53].

The case of nonzero next-nearest-neighbor interactions, nonzero \tilde{J}_{z2} , has been studied numerically in Ref. [53] and with mean-field theory in Refs. [54–56]. For example, in Ref. [53], it is shown that, for a certain parameter range satisfying $\tilde{J}_{z2} \gtrsim \tilde{J}_{z1} > 0$ and $\tilde{J}_{z2} \gtrsim \tilde{J}_\perp > 0$, it is energetically favorable for the plaquettes to arrange themselves in a striped solid. Assuming, by analogy, that $|\tilde{J}_{z2}| \gtrsim |\tilde{J}_{z1}|$ and $|\tilde{J}_{z2}| \gtrsim |\tilde{J}_\perp|$ are both necessary for a new phase to appear, no such phase can occur in the perturbative phase diagram for the t - J_\perp Hamiltonian since this set of conditions is never satisfied. Furthermore, near the phase transition boundaries for this phase diagram, the magnitude of \tilde{J}_{z2} is about an order of magnitude smaller than the magnitude of \tilde{J}_{z1} . We therefore expect \tilde{J}_{z2} to have an insignificant effect on the locations of phase transitions, so we neglect \tilde{J}_{z2} for the remainder of the paper.

The condition for a phase transition $\pm|\tilde{J}_\perp| = \tilde{J}_{z1}$ is thus

$$\pm 2|g_t^{(4,2)}| = f_t^{(2,2)} - 2f_t^{(4,2)} + \left(\frac{J'_\perp}{t'}\right)^2 (f_\perp^{(2,2)} + f_\perp^{(4,4)} - 2f_\perp^{(4,2)}). \quad (13)$$

Here, a transition between superfluid and checkerboard solid occurs for $+$, a transition between superfluid and phase

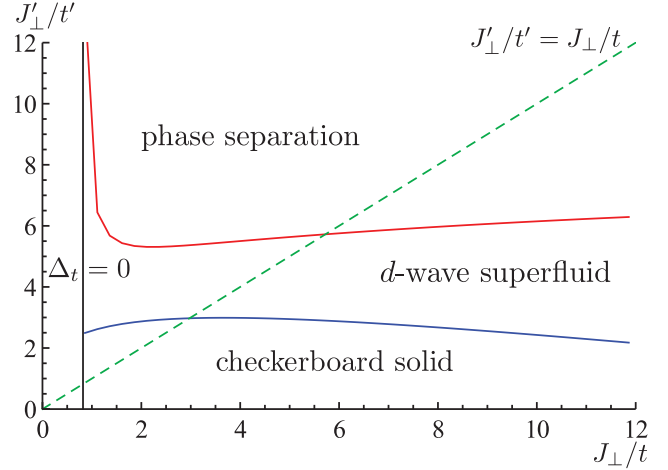


FIG. 3. (Color online) Phase diagram for the t - J_\perp Hamiltonian. The region to the right of the vertical black line is the region where $\Delta_t > 0$. The line $J'_\perp/t' = J_\perp/t$ is shown as a dashed green line and passes through all three phases.

separation occurs for $-$, and the functions are evaluated at J_\perp/t . By solving Eq. (13), the phase diagram in the original variables J_\perp/t and J'_\perp/t' is computed in the region $\Delta_t > 0$ and is shown in Fig. 3. All three phases are present in this phase diagram and the d -wave superfluid phase exists for a large range of values of J_\perp/t and J'_\perp/t' . The easiest case to study experimentally is $t' = t$ and $J'_\perp = J_\perp$, which is outside the validity of this perturbative calculation. However, as a guess as to the physics for these values of t' and J'_\perp , it is useful to consider the line $J'_\perp/t' = J_\perp/t$. As is shown in Fig. 3, this line passes through all three phases, indicating that all three phases might be observable in the simplest t - J_\perp experiment with a homogeneous lattice.

There is a strong indication that the qualitative features of our results may be relevant to the nonperturbative regime where $J'_\perp/t' = J_\perp/t$. Specifically, the phase diagram along the line $J'_\perp/t' = J_\perp/t$ in Fig. 3 is qualitatively similar to the phase diagram along the line of $1/4$ hole density in Fig. 4 of Ref. [57], which numerically studies the standard t - J model. Indeed, the order of the phases in the two diagrams is the same provided that one identifies the region of uncondensed bound holes in Ref. [57] with our checkerboard solid phase and the Fermi liquid in Ref. [57] with our region $\Delta_t < 0$.

IV. ANALYSIS OF THE EFFECTS OF J_z , V , AND W

In this section, we analyze the effects of J_z , V , and W on the d -wave superfluid phase. First in Sec. IV A, we repeat the single-plaquette analysis of Sec. III A for various Hamiltonians with nonzero J_z , V , and W . In Sec. IV C, we then compute the phase diagrams using the methods of Sec. III B for those Hamiltonians capable of exhibiting d -wave superfluidity.

A. Single-plaquette solutions

First, we examine the Hamiltonian with independent J_\perp and J_z and zero V and W , the t - J_\perp - J_z Hamiltonian. Contour plots of the binding energy Δ_t and $|\langle 4|\Delta_d^\dagger|2\rangle|$ for this Hamiltonian are shown in Fig. 4. From these figures we see that $\Delta_t > 0$ and $|\langle 4|\Delta_d^\dagger|2\rangle| \neq 0$ for most values of $J_\perp/t > 0$ and $J_z/t > 0$.

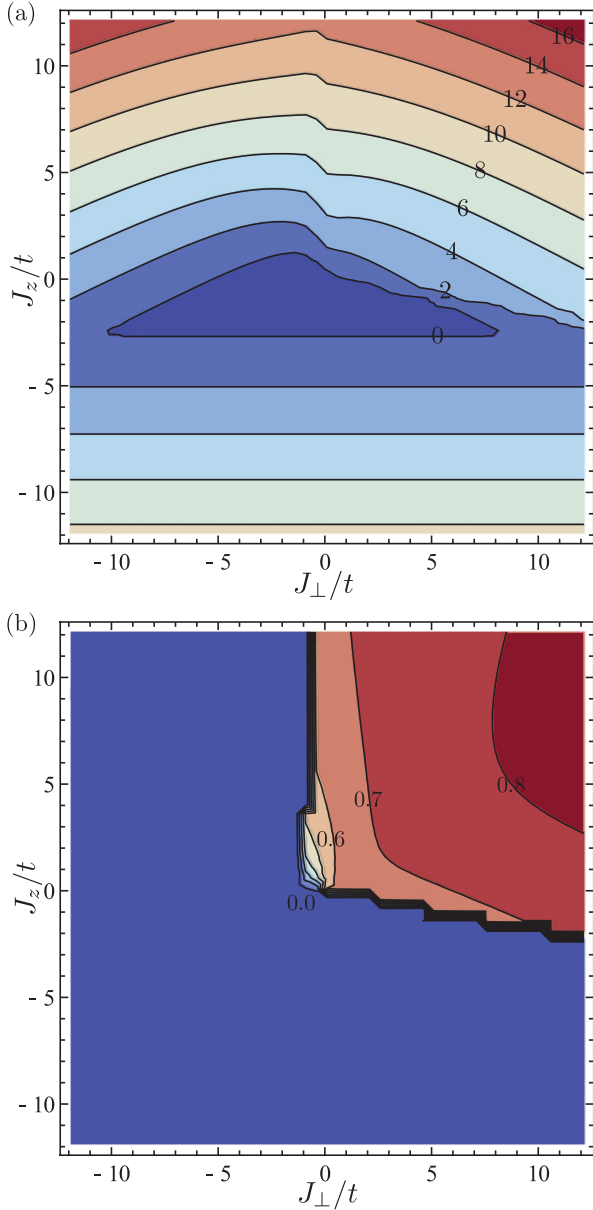


FIG. 4. (Color online) Single-plaquette analysis for the t - J_\perp - J_z Hamiltonian. (a) Binding energy Δ_r . Contours of constant Δ_r/t are labeled. (b) Matrix element $|\langle 4 | \Delta_d^\dagger | 2 \rangle|$. Contours of constant $|\langle 4 | \Delta_d^\dagger | 2 \rangle|$ are labeled.

The $|4\rangle$ ground states in the A_2 and B_1 representations for positive J_z/t are

$$|2,2(A_2)\rangle = \frac{1}{\sqrt{2}} (|\uparrow\downarrow\uparrow\downarrow\rangle - |\downarrow\uparrow\downarrow\uparrow\rangle),$$

$$|2,2(B_1)\rangle = \frac{1}{\sqrt{2}} (|\uparrow\downarrow\uparrow\downarrow\rangle + |\downarrow\uparrow\downarrow\uparrow\rangle) + O\left(\frac{J_\perp}{t}\right).$$

Thus, for positive J_z/t and along the line $J_\perp/t = 0$, the two alternating spin configurations are the twofold degenerate $|4\rangle$ ground states. When J_\perp/t is made nonzero but small, the symmetric combination of these two states, which has B_1 symmetry, becomes the nondegenerate ground state.

Next, we examine the Hamiltonian with independent $J_\perp = J_z = J$ and W and zero V , the t - J - W Hamiltonian.

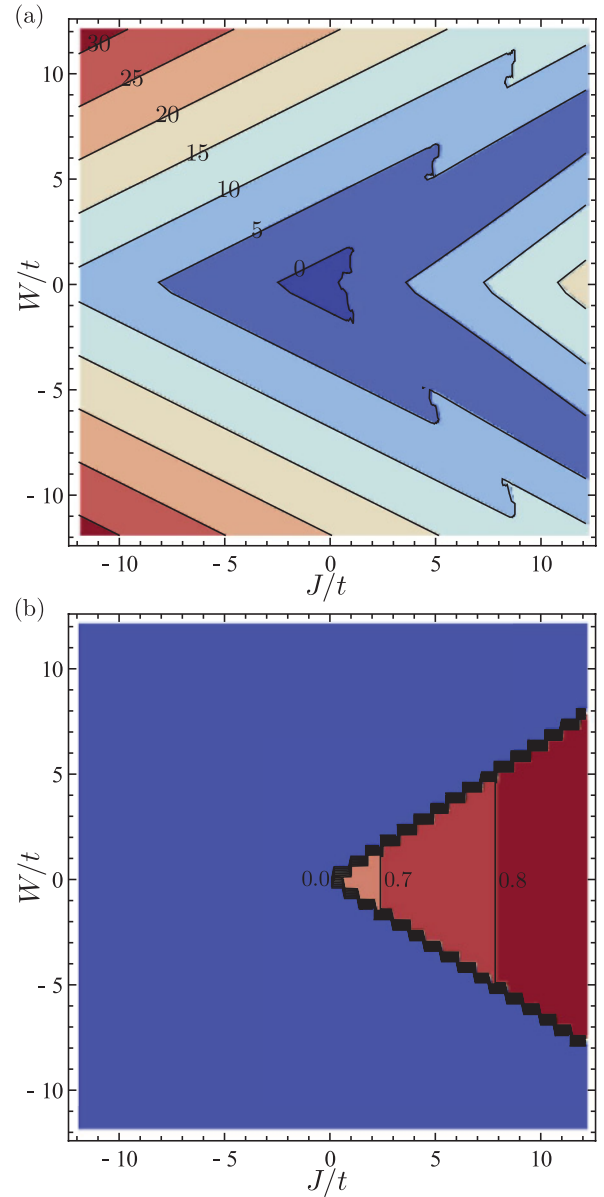


FIG. 5. (Color online) Single-plaquette analysis for the t - J - W Hamiltonian with $J_\perp = J_z = J$. (a) Binding energy Δ_r . Contours of constant Δ_r/t are labeled. (b) Matrix element $|\langle 4 | \Delta_d^\dagger | 2 \rangle|$. Contours of constant $|\langle 4 | \Delta_d^\dagger | 2 \rangle|$ are labeled.

Contour plots of the binding energy Δ_r and $|\langle 4 | \Delta_d^\dagger | 2 \rangle|$ for this Hamiltonian are shown in Fig. 5. From these figures we see that $\Delta_r > 0$ and $|\langle 4 | \Delta_d^\dagger | 2 \rangle| \neq 0$ for most values of $J/t > 0$ and W/t approximately between the lines $W/t = \pm 2J/3t$.

This behavior can be explained by considering the ground-state configurations and symmetries of $|2\rangle$ and $|4\rangle$ shown in Fig. 6. If W is large and positive, all of the spins will point down in the single-plaquette ground states: the $|2\rangle$ ground state is a p wave $|0,2\rangle$ and the $|4\rangle$ ground state is a d wave $|0,4\rangle$. For $W = 0$ and $J/t > 0$, it is energetically favorable to have an equal number of spin-up and spin-down molecules on each plaquette, and the $|2\rangle$ ground state is an s wave $|1,1\rangle$, while the $|4\rangle$ ground state is a d wave $|2,2\rangle$. As W is decreased from a large positive value (and $J_\perp/t > 0$), the $|2\rangle$ ground state

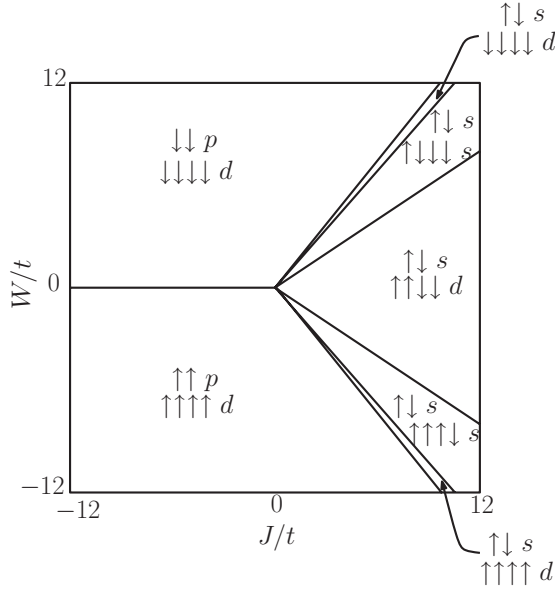


FIG. 6. Configurations of the single-plaquette ground states for two and four molecules for the t - J - W Hamiltonian with $J_{\perp} = J_z = J$.

first switches from $|0,2\rangle$ to an s wave $|1,1\rangle$, and then the $|4\rangle$ ground state switches from $|0,4\rangle$ to an s wave $|1,3\rangle$. As W is further decreased, the $|4\rangle$ ground state switches to a d -wave symmetric $|2,2\rangle$. As W is made large and negative, the process repeats with up spins replacing down spins. $\langle 4|\Delta_d^{\dagger}|2\rangle$ vanishes for W/t approximately outside the lines $W/t = \pm 2J/3t$ since the $|4\rangle$ ground state switches from d wave to s wave outside this region. In particular, $\langle 4|\Delta_d^{\dagger}|2\rangle = 0$ in the narrow region where the ground states are s wave $|1,1\rangle$ and d wave $|1,3\rangle$ because Δ_d^{\dagger} creates one up spin and one down spin.

We do not consider Hamiltonians with nonzero V here since they do not support d -wave superfluidity in our perturbative calculations as is described in the following section. We also note that, similar to the t - J_{\perp} model where Δ_{40} becomes negative at large J_{\perp}/t , the region where a lattice of $|2\rangle$ s and $|4\rangle$ s is the true ground state is also limited in the models discussed in this section. However, as in the case of the t - J_{\perp} model, the full phase diagrams discussed in Sec. IV C can still be accessed in experiments with ultracold polar molecules by adiabatic preparation starting with suitable initial states.

B. First-order contributions to the XXZ effective Hamiltonian

In this section, we examine the question of which of the Hamiltonians defined by Eq. (1) have nonzero first-order contributions to the XXZ effective Hamiltonian. A first-order shift in the ground-state energies, a nonzero H_{1g} in Eq. (6), would contribute to, and generally dominate, the diagonal terms $f^{(4,2)}$, $f^{(2,2)}$, $f^{(4,4)}$, $h^{(4,2)}$, $h^{(2,2)}$, and $h^{(4,4)}$ but not the off-diagonal term $g^{(4,2)}$. Since the order $(t'/t)^2$ function $g^{(4,2)}$ is the only function contributing to \tilde{J}_{\perp} [Eq. (12a)], \tilde{J}_{\perp} will generally be small compared to \tilde{J}_{z1} and \tilde{J}_{z2} [Eqs. (12b) and (12c)], if there are nonzero first-order contributions. Thus, this perturbative analysis predicts no robust superfluid phase if there are nonzero first-order contributions to the effective Hamiltonian. Therefore, we will not compute the phase

diagram for those Hamiltonians that contribute first-order corrections. Note that there are no first-order shifts in the t - J_{\perp} Hamiltonian studied in Sec. III.

To study when first-order contributions arise, we consider here the effects of the J'_z , V' , and W' terms separately. Since these terms cannot couple $|2\rangle|4\rangle$ to $|4\rangle|2\rangle$, they will only contribute to the diagonal matrix elements of H_{eff} . Let R and R' label the plaquettes containing sites r and r' , respectively, and let $n_{R\sigma}$ denote the number of molecules with spin σ on plaquette R . Due to the D_4 symmetry, any single-plaquette eigenstate $|n_{R\uparrow}, n_{R\downarrow}\rangle$ that is nondegenerate within the manifold of states with constant $n_{R\uparrow}$ and $n_{R\downarrow}$ satisfies

$$\langle n_{R\uparrow}, n_{R\downarrow} | n_{r\sigma} | n_{R\uparrow}, n_{R\downarrow} \rangle = \frac{1}{4} n_{R\sigma}. \quad (14)$$

First, consider the V' term. From Eq. (14), the state $|n_R\rangle |n_{R'}\rangle$ satisfies

$$\langle n_r n_{r'} \rangle = \frac{1}{16} n_R n_{R'},$$

where $n_r = n_{r\uparrow} + n_{r\downarrow}$ and $n_R = n_{R\uparrow} + n_{R\downarrow}$. Thus the V' contributions vanish to first order if and only if at least one of the two interacting plaquettes is empty. Since the effective Hamiltonian is constructed from $|2\rangle$ and $|4\rangle$ plaquettes, the V' term will always contribute to first order and will not be considered further here. It is important to emphasize that our analysis should be considered to be exactly valid only in our perturbative regime, since it is believed that the t - J model, which contains nonzero V' , supports d -wave superfluidity [1–3, 57, 58].

Next, consider the J'_z term. Since $S_r^z = (n_{r\uparrow} - n_{r\downarrow})/2$, the state $|n_{R\uparrow}, n_{R\downarrow}\rangle |n_{R'\uparrow}, n_{R'\downarrow}\rangle$ satisfies

$$\langle S_r^z S_{r'}^z \rangle = \frac{1}{64} (n_{R\uparrow} - n_{R\downarrow})(n_{R'\uparrow} - n_{R'\downarrow}).$$

Thus, the J'_z contributions vanish to first order if and only if at least one of the two interacting plaquettes satisfies $n_{\uparrow} = n_{\downarrow}$. In all of the regions identified in Sec. IV A as possibly supporting d -wave superfluidity in the t - J_{\perp} - J_z Hamiltonian, $|2\rangle$ and $|4\rangle$ have this property. Therefore, J'_z never contributes at first order in the parameter regimes that we are interested in for this Hamiltonian.

Finally, consider the W' term. The state $|n_{R\uparrow}, n_{R\downarrow}\rangle |n_{R'\uparrow}, n_{R'\downarrow}\rangle$ satisfies

$$\langle n_r S_{r'}^z + n_{r'} S_r^z \rangle = \frac{1}{16} (n_{R\uparrow} n_{R'\uparrow} - n_{R\downarrow} n_{R'\downarrow}).$$

Thus the W' contributions vanish to first order if and only if the two interacting plaquettes satisfy $n_{R\uparrow} n_{R'\uparrow} = n_{R\downarrow} n_{R'\downarrow}$. From Fig. 6, we see that this condition is met for $|2\rangle|4\rangle$, $|2\rangle|2\rangle$ and $|4\rangle|4\rangle$ only for the region where the $|2\rangle$ ground state is s -wave symmetric $|1,1\rangle$ and the $|4\rangle$ ground state is d -wave symmetric $|2,2\rangle$. We also note that the condition $n_{\uparrow} = n_{\downarrow}$, necessary for the J'_z contributions to vanish at first order, is satisfied by both $|2\rangle$ and $|4\rangle$ in this region. Notice, however, that the condition $n_{\uparrow} = n_{\downarrow}$ is not satisfied by the $|4\rangle$ states outside this region. Thus, not only W' but also J'_z will give nonzero first-order contributions outside this region.

While other regions in Fig. 6 cannot exhibit a d -wave superfluid within our analysis, they may still exhibit interesting phases at appropriate filling fractions. For example, the regions where the ground states are $|1,1\rangle$ and $|0,4\rangle$ or $|4,0\rangle$ might

support a *d*-wave solid phase with an asymmetry between up and down spins, while the regions where the ground states are $|1,1\rangle$ and $|1,3\rangle$ or $|3,1\rangle$ might support an *s*-wave solid phase. However, we will not discuss such phases further and will focus, instead, on the parameter space that has no first-order corrections and that is, therefore, capable of exhibiting *d*-wave superfluidity.

C. Phase diagrams

We first consider the general t - J_{\perp} - J_z Hamiltonian. There are four independent parameters, J_{\perp}/t , J_z/t , J'_{\perp}/t' , and J'_z/t' , so the phase diagram is four dimensional. Notice that, within the perturbative treatment, the fifth parameter t'/t affects only the overall energy scale but not the phase diagram. In order to plot a manageable phase diagram, we restrict the parameter space to $J'_{\perp}/t' = J_{\perp}/t$ and $J'_z/t' = J_z/t$. Using the expressions for \tilde{J}_{\perp} and \tilde{J}_{z1} given by Eq. (12) and the generalization of Eq. (8) to include J_z and J'_z , we find the phase boundaries by solving $|\tilde{J}_{\perp}| = |\tilde{J}_{z1}|$. The resulting phase diagram is shown in Fig. 7. As is discussed in Sec. IV A, along the J_z/t axis, the $|4\rangle$ ground state becomes doubly degenerate. Thus, the effective Hamiltonian no longer maps to an *XXZ* Hamiltonian, and we do not compute the phase diagram along this line. In the absence of the hardcore constraint, the t - J_z Hamiltonian on a homogeneous lattice is studied in Ref. [32]. The t - J_{\perp} phase diagram along the green dashed line $J'_{\perp}/t' = J_{\perp}/t$ shown in Fig. 3 corresponds to the phase diagram along the J_{\perp}/t axis in Fig. 7. For values of J_z/t greater than about 1, the checkerboard solid phase is no longer present, and for values of J_z/t greater than about 2, the superfluid phase is no longer present. We see that large values of J_z have the effect of reducing the areas of the checkerboard solid and superfluid phases. However, by tuning J_z/t to a value between about 1 and 2, the extent of the *d*-wave superfluid phase along the J_{\perp}/t direction is increased relative to its value without the J_z interaction. This is achieved by the suppression of the

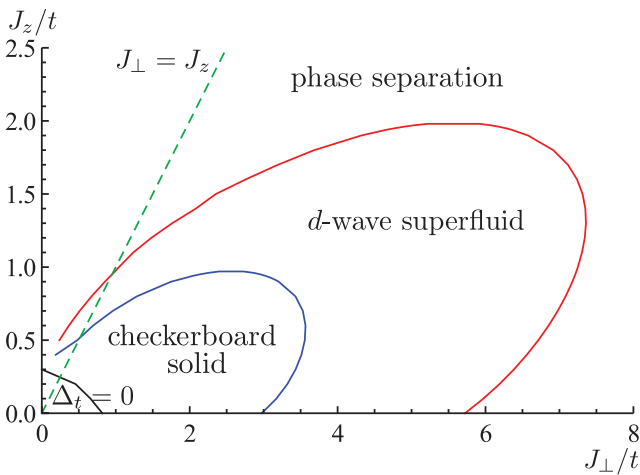


FIG. 7. (Color online) Phase diagram for the t - J_{\perp} - J_z Hamiltonian assuming $J'_{\perp}/t' = J_{\perp}/t$ and $J'_z/t' = J_z/t$. The region above the black curve is the region where $\Delta_t > 0$. The SU(2)-symmetric Hamiltonian with $J_{\perp} = J_z$ is shown by the dashed green line. We do not compute the phase diagram along the J_z/t axis since the $|4\rangle$ ground state is degenerate here.

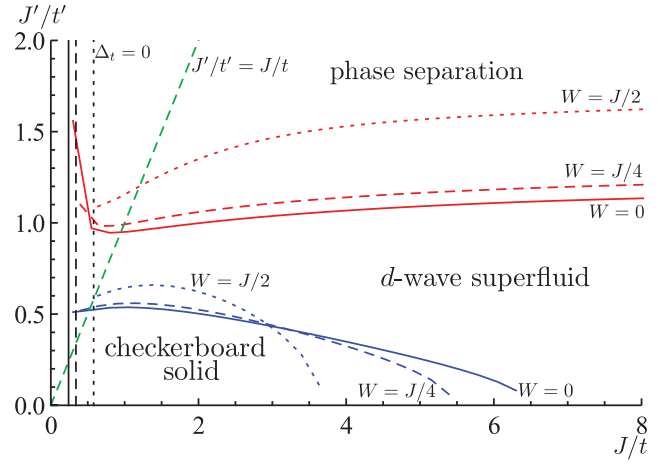


FIG. 8. (Color online) Phase diagram for the t - J - W Hamiltonian for $J_{\perp} = J_z = J$. Phase transitions for $W = 0$ [the SU(2)-symmetric t - J_{\perp} - J_z Hamiltonian] are shown in solid lines, transitions for $W = J/4$ are shown in dashed lines, and transitions for $W = J/2$ are shown in dotted lines. The regions to the right of the vertical black lines are the regions where $\Delta_t > 0$ for these three values of W . The line $J'/t' = J/t$ is shown as a dashed green line.

checkerboard solid and phase separation phases at small J_{\perp}/t and large J_{\perp}/t , respectively.

We next consider the phase diagram for the SU(2)-symmetric t - J_{\perp} - J_z Hamiltonian with $J_{\perp} = J_z = J$ shown in Fig. 8 as solid lines. The phase diagram along the green dashed line $J'/t' = J/t$ in Fig. 8 for the SU(2)-symmetric t - J_{\perp} - J_z Hamiltonian corresponds to the phase diagram along the green dashed line $J_{\perp} = J_z$ in Fig. 7. The regions not in phase separation are reduced from those for the t - J_{\perp} Hamiltonian (see Fig. 3). The fact that J_z reduces the superfluid phase for the SU(2)-symmetric case is to be expected from Fig. 7 since the line $J_{\perp} = J_z$ does not pass through the regions where the superfluid phase is enhanced by the presence of J_z .

Finally, we add W and consider the phase diagram for the t - J - W Hamiltonian with $J_{\perp} = J_z = J$ shown in Fig. 8. The phase diagram is shown along the lines $W = 0$ (discussed above), $W = J/4$, and $W = J/2$, which are contained within the region where $|2\rangle$ is an *s*-wave symmetric $|1,1\rangle$ and $|4\rangle$ is a *d*-wave symmetric $|2,2\rangle$ (see Fig. 6). Increasing W moves the transition between the superfluid and phase separation phases up along the J'/t' axis and therefore slightly increases the region of *d*-wave superfluidity. Increasing W also decreases the extent of the checkerboard solid phase along the J/t axis.

In summary, within our treatment, Hamiltonians involving V do not support superfluidity. At the same time, we identify regions of parameter space where J_z and W enhance the *d*-wave superfluid phase.

V. EXPERIMENTAL REALIZATIONS OF THE PERTURBATIVE CALCULATION

The perturbative results obtained above can be regarded only as a qualitative guess as to the behavior of the simplest homogeneous square lattice since intraplaquette and interplaquette couplings are equal in this case. Therefore, in this section, we propose experimental configurations

accurately described by our perturbative analysis. In Sec. V A, we describe a one-dimensional stack of plaquettes. Then, in Sec. V B, we briefly describe an experimentally more challenging two-dimensional configuration.

A. One-dimensional stack of plaquettes

As shown in Fig. 9, we propose to apply a dc electric field in the vertical (\hat{z}) direction. We then propose to stack plaquettes with sides of length a on top of each other along \hat{z} a distance a' apart. The strength of dipolar interactions between two molecules is proportional to

$$\frac{1 - 3 \cos^2 \theta}{r^3}, \quad (15)$$

where r is the distance between the molecules and θ is the angle made between the line connecting the molecules and the external dc electric field. Due to the $1/r^3$ dependence, interplaquette dipolar interactions can be treated perturbatively relative to the intraplaquette interactions provided $a' \gg a$. One way of achieving this geometry experimentally is to use different frequency lasers to create the optical lattices in the plane and in the vertical direction. The distances a and a' can also be controlled by varying the angle at which the lasers interfere [59,60] or by holographic techniques [61].

The plaquettes can be made by interfering lasers of wavelength $2a$ and $4a$ to create a superlattice [9] such that tunneling between plaquettes in a plane is negligible. To avoid in-plane interplaquette dipole-dipole interactions, molecules in neighboring stacks may have to be removed. The required addressability can be achieved by applying temporary additional light shifts or electric field gradients. Alternatively, instead of emptying neighboring stacks, an extreme version of the superlattice can be used to separate the stacks enough to make both the tunneling and the dipolar interactions between them negligible.

As is shown in Fig. 9, with this geometry, there is a hopping amplitude t between nearest neighbors within a plaquette and a hopping amplitude t' along \hat{z} between nearest-neighbor plaquettes. The amplitudes t and t' can be controlled separately

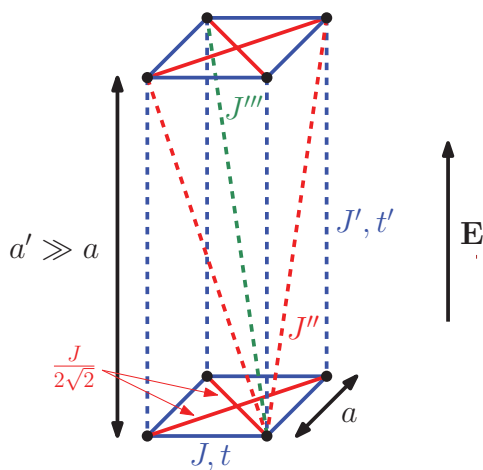


FIG. 9. (Color online) Geometry of the one-dimensional stack of plaquettes. The external dc electric field is perpendicular to the plaquettes.

by varying the intensities of the lasers making the lattices in each direction. There are five strengths, two within a plaquette and three between plaquettes, of the dipolar interactions J_{\perp} , J_z , V , and W discussed here generically as J . As shown in Fig. 9, let J be the strength of dipolar interactions between nearest neighbors within a plaquette, and let J' , J'' , and J''' be the strengths of the dipolar interactions between plaquettes. The ratios J'/J , J''/J , and J'''/J are functions of the ratio a'/a and are controlled separately from the ratio t'/t . For $a' > a$, by Eq. (15), J' , J'' , and J''' are the opposite sign of J .

1. Phase diagrams

For a one-dimensional stack of plaquettes, we calculate the same phase diagrams computed above for the two-dimensional lattice of plaquettes. In an experiment with one independent dipolar interaction strength J , there are three independent parameters: J/t , a'/a , and t'/t or, equivalently, J/t , J'/t' , and a'/a . In order to compare with the phase diagrams computed above, we choose the latter set of parameters. It is currently possible to use lasers of wavelength 1064 nm to produce optical lattices with spacing $a' = 532$ nm. Assuming that it is also possible to use a second wavelength in the range 400–600 nm, in the following phase diagrams, we use $a'/a = 5/2$. For $a'/a = 5/2$, $J'/J = -0.128$, $J''/J = -0.081$, and $J'''/J = -0.054$.

The phase diagram for the t - J_{\perp} Hamiltonian is shown in Fig. 10. Since it is possible with this scheme to control J'_{\perp}/t' by varying a'/a and t'/t , we plot the lines $-J'_{\perp}/t' = J_{\perp}/2t$, $-J'_{\perp}/t' = J_{\perp}/t$, and $-J'_{\perp}/t' = 2J_{\perp}/t$ in Fig. 10. This phase diagram is qualitatively similar to the corresponding phase diagram for the two-dimensional case (Fig. 3). However, the overall vertical scale of the phase diagram is increased for the stack resulting in a larger region of d -wave superfluidity. The increase in the vertical scale can be explained by the presence of the J'_{\perp} and J''_{\perp} terms, which reduce the f_{\perp} functions relative to the f_t and g_t functions in Eq. (8). Thus, a larger value of J'_{\perp}/t' is needed to reach the phase boundaries.

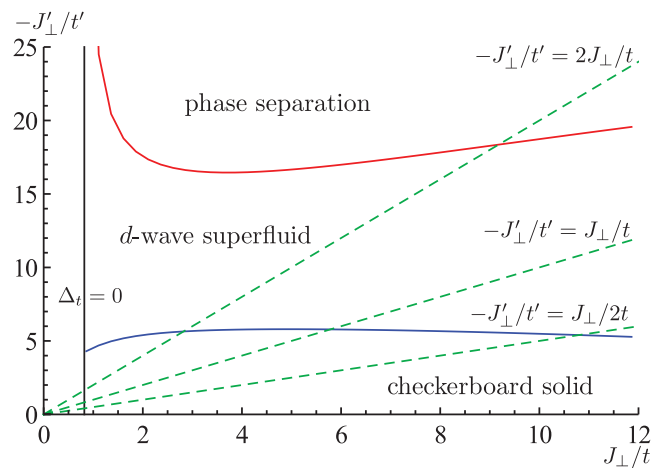


FIG. 10. (Color online) Phase diagram for the t - J_{\perp} Hamiltonian for a one-dimensional stack of plaquettes with $a'/a = 5/2$. Regions to the right of the vertical black line are where $\Delta_t > 0$. The lines $-J'_{\perp}/t' = J_{\perp}/2t$, $-J'_{\perp}/t' = J_{\perp}/t$, and $-J'_{\perp}/t' = 2J_{\perp}/t$ are shown by the green dashed lines.

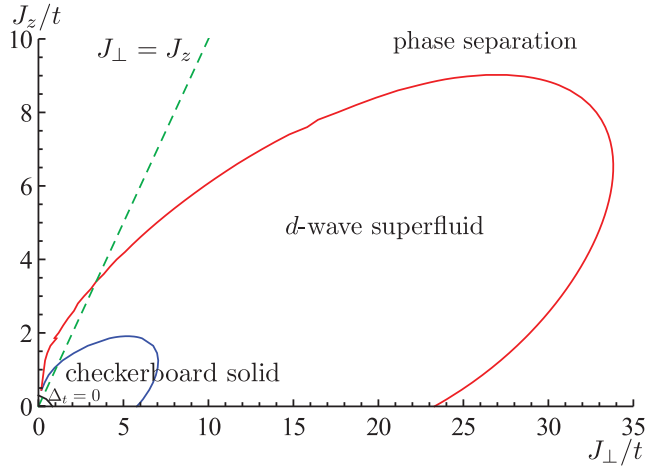


FIG. 11. (Color online) Phase diagram for the t - J_{\perp} - J_z Hamiltonian assuming $J'_{\perp}/t' = J_{\perp}/t$ and $J'_z/t' = J_z/t$ for a one-dimensional stack of plaquettes with $a'/a = 5/2$. The region above the black curve is the region where $\Delta_t > 0$. The SU(2)-symmetric Hamiltonian with $J_{\perp} = J_z$ is shown by the dashed green line.

We refer the reader to Appendix A3 for a symmetry-based explanation for why J''_{\perp} and J'''_{\perp} reduce the f_{\perp} functions. Similar arguments hold for the increased scales in the t - J_{\perp} - J_z and the t - J - W phase diagrams discussed below.

The phase diagram for the t - J_{\perp} - J_z Hamiltonian with $J'_{\perp}/t' = J_{\perp}/t$ and $J'_z/t' = J_z/t$ is shown in Fig. 11. This phase diagram is qualitatively similar to the corresponding phase diagram for the two-dimensional case shown in Fig. 7. As with the two-dimensional case, J_z can increase the superfluid phase.

The phase diagram for the SU(2)-symmetric t - J_{\perp} - J_z Hamiltonian is shown in Fig. 12 as solid lines. Again, the diagram is qualitatively similar to its counterpart for the two-dimensional system (Fig. 8) with the range of J'/t' not in the phase-separation regime increased.

The overall scale of the phase diagram in Fig. 11 is increased from the corresponding diagram for the two-dimensional system shown in Fig. 7 as is expected from Figs. 10 and 12. The t - J_{\perp} phase diagram along the middle green dashed line $-J'_{\perp}/t' = J_{\perp}/t$ shown in Fig. 10 corresponds to the phase diagram along the J_{\perp}/t axis in Fig. 11. The SU(2)-symmetric phase diagram along the middle green dashed line $-J'/t' = J/t$ shown in Fig. 12 corresponds to the phase diagram along the green dashed line $J_{\perp} = J_z$ in Fig. 11. Since both of these green lines in Figs. 10 and 12 pass through larger regions of the superfluid phase than in the corresponding phase diagrams for the two-dimensional plane (Figs. 3 and 8), the overall scale of the t - J_{\perp} - J_z phase diagram (Fig. 11) increases. The superfluid phase can be further increased by decreasing the slope of the line relating J'_{\perp}/t' (J'/t') and J_{\perp}/t (J/t) in Fig. 10 (Fig. 12) since lines with shallower slopes pass through larger regions of the superfluid phase.

The phase diagram for the t - J - W Hamiltonian for $J_{\perp} = J_z = J$ is shown in Fig. 12. In contrast to the phase diagram for the two-dimensional t - J - W Hamiltonian, in the stack geometry, an increase in W moves the transition between the superfluid and phase separation phases down rather than up, thus reducing the superfluid phase. Furthermore, in the stack

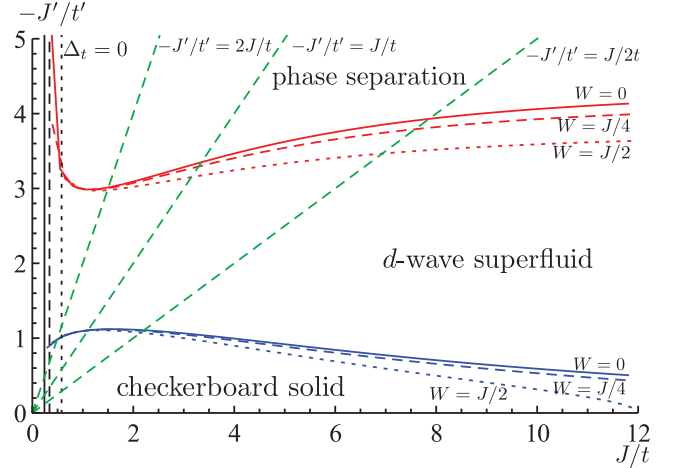


FIG. 12. (Color online) Phase diagram for the t - J - W Hamiltonian for $J_{\perp} = J_z = J$ for a one-dimensional stack of plaquettes with $a'/a = 5/2$. Phase transitions for $W = 0$ [the SU(2)-symmetric t - J_{\perp} - J_z Hamiltonian] are shown in solid lines, transitions for $W = J/4$ are shown in dashed lines, and transitions for $W = J/2$ are shown in dotted lines. The regions to the right of the vertical black lines are the regions where $\Delta_t > 0$ for these three values of W . The lines $-J'/t' = J/2t$, $-J'/t' = J/t$, and $-J'/t' = 2J/t$ are shown by the green dashed lines.

geometry, an increase in W only slightly decreases the extent of the checkerboard solid phase. Thus, for the stack of plaquettes, the W term can slightly increase the superfluid region only for small $|J'/t'|$.

2. Preparation and detection

Since there are no strong relaxation mechanisms in optical lattice experiments using cold atoms and molecules, it is not an easy task to prepare the ground state of a given Hamiltonian. One strategy is to prepare an easier state that is the ground state of another Hamiltonian and to adiabatically change that Hamiltonian to the desired one [9,48,62,63]. Here we consider the adiabatic preparation of the d -wave superfluid phase at the point where $\tilde{J}_{z1} = 0$ for the t - J_{\perp} Hamiltonian. This corresponds to preparing the ground state of the XX magnet. We propose first adiabatically preparing $|2\rangle$ and $|4\rangle$ states alternating in a stack and then adiabatically preparing the ground state of the t - J_{\perp} Hamiltonian. The preparation of the ground state of the XX magnet is similar to the method described in Ref. [62] for adiabatically preparing the ground state of the Heisenberg antiferromagnet.

First, consider bringing the plaquettes far apart to avoid interplaquette interactions and preparing the $|2\rangle$ and $|4\rangle$ ground states alternating along the stack. Let H_0 be the t - J_{\perp} Hamiltonian on a single plaquette and consider the following single-plaquette Hamiltonians:

$$H_2(\tau) = H_0 - B(\tau) (S_1^z - S_3^z), \quad (16)$$

$$H_4(\tau) = H_0 - B(\tau) (S_1^z + S_2^z - S_3^z - S_4^z), \quad (17)$$

used to prepare the $|2\rangle$ and $|4\rangle$ ground states, respectively. Here $B(\tau)$ is the strength of an effective alternating magnetic field on the sites of the plaquette as a function of time τ . For large positive values of $B(\tau)$, the ground state of H_2 for two

molecules is up on 1 and down on 3, while the ground state of H_4 for four molecules is up on 1 and 2 and down on 3 and 4. These states can be prepared using single-site addressability provided by electric field gradients or high-resolution optics [6,7]. For values of J_\perp/t of interest, in a plaquette with two molecules, the energy gap between the ground state and first excited state of H_2 never closes as $B(\tau)$ is reduced to zero. The same is true of H_4 for a plaquette with four molecules. Thus, the $|2\rangle$ and $|4\rangle$ ground states of the $t-J_\perp$ Hamiltonian can be prepared by adiabatically reducing the effective magnetic field $B(\tau)$ from some large initial value to zero in H_2 and H_4 , respectively. Once the $|2\rangle$ and $|4\rangle$ ground states have been prepared, the plaquettes can be brought to a distance a' from each other by changing the angle at which the lasers interfere or by holographic techniques.

Once the $|2\rangle$ and $|4\rangle$ ground states have been prepared, the ground state of the $t-J_\perp$ Hamiltonian at the point $\tilde{J}_{z1} = 0$ can be prepared by adiabatically turning off the effective magnetic field $\tilde{B}(\tau)$ acting on the effective spins $|\uparrow\rangle$ and $|\downarrow\rangle$ in the Hamiltonian

$$H(\tau) = \tilde{J}_\perp \sum_R (S_R^X S_{R+1}^X + S_R^Y S_{R+1}^Y) + \tilde{B}(\tau) \sum_R (-1)^R S_R^Z. \quad (18)$$

The first term is just the XXZ effective Hamiltonian Eq. (11) at the point $\tilde{J}_{z1} = 0$, while the second term describes an alternating effective magnetic field between plaquettes along the Z direction. The energy gap between the ground state and the first excited state of the Hamiltonian Eq. (18) decreases monotonically with decreasing magnetic field but never closes, so the d -wave superfluid phase can, in principle, be prepared by adiabatically turning off $\tilde{B}(\tau)$. However, for a stack of N plaquettes, the energy gap between the ground state and the first excited state of the XX chain is proportional to $1/N$. Although it is outside the scope of the present paper, the ideal $\tilde{B}(\tau)$ over a given time T can be calculated by mapping Eq. (18) to free fermions and maximizing the superfluid order parameter when $\tilde{B}(T) = 0$. Since the energy gap is large for large $\tilde{B}(\tau)$ and only scales as $1/N$ for small $\tilde{B}(\tau)$, it is likely that this ideal $\tilde{B}(\tau)$ decreases rapidly initially and more slowly at later times.

As a rough estimate for the minimum time T necessary to prepare the superfluid phase at the point $\tilde{J}_{z1} = 0$, we estimate $T = N/\tilde{J}_\perp$. The strength of the dipole-dipole interactions at a distance of 200 nm is roughly $J_\perp \approx 2\pi \times 4$ kHz for the molecule KRb. The value of $J'_\perp \approx -2\pi \times 500$ Hz is then fixed by the ratio a'/a . t is chosen such that \tilde{J}_\perp is as large as possible while perturbation theory is valid. t' is chosen such that $\tilde{J}_{z1} = 0$. Then for $J_\perp/t = 4$, $t \approx 2\pi \times 1$ kHz and $\tilde{J}_{z1} = 0$ requires $t' \approx 2\pi \times 300$ Hz. At this point, $\tilde{J}_\perp \approx 2\pi \times 1.5$ Hz so $T \approx 100N$ ms. For these parameters, $\Delta_t \approx 2\pi \times 2$ kHz and $\Delta_\perp \approx 2\pi \times 4$ kHz so the conditions $t' \ll \Delta_t$ and $J'_\perp \ll \Delta_\perp$ are met, and perturbation theory is valid. Using the inverse gap at $B(\tau) = 0$ in Eqs. (16) and (17) gives $400 \mu\text{s}$ as a rough estimate for the minimum time necessary to prepare the $|2\rangle$ and $|4\rangle$ ground states. Thus, as expected, the preparation time is dominated by the preparation of the ground state of the XX chain. Therefore, assuming an optimistic coherence time of 1 s, roughly 10 plaquettes can be prepared. For LiCs,

$J_\perp \approx 2\pi \times 400$ kHz at a distance of 200 nm allowing roughly 10^3 plaquettes to be prepared in 1 s. These numbers can be improved by reducing the ratio a'/a or by preparing a superfluid away from the point $\tilde{J}_{z1} = 0$.

The effective magnetic fields in Eqs. (16)–(18) can be created using tensor shifts [18,21,24,30,43,64] and superlattices [9] so that up- and down-spins (both the initial $|\uparrow\rangle$ and $|\downarrow\rangle$ and the effective $|\uparrow\rangle$ and $|\downarrow\rangle$) have different potential energies.

The d -wave superfluid phase can be detected via second-order noise correlations in the expanding molecular cloud which is proportional to the the four-point function

$$G_{\sigma\sigma'}(\mathbf{Q}, \mathbf{Q}') \propto \langle n_\sigma(\mathbf{Q}) n_{\sigma'}(\mathbf{Q}') \rangle - \langle n_\sigma(\mathbf{Q}) \rangle \langle n_{\sigma'}(\mathbf{Q}') \rangle$$

at the time the molecules are released from the trap [37,65,66]. Here

$$n_\sigma(\mathbf{Q}) \propto \sum_{r,r'} e^{i\mathbf{Q}\cdot\mathbf{L}_{rr'}} c_{r\sigma}^\dagger c_{r'\sigma}$$

is the quasimomentum distribution and $\mathbf{L}_{rr'}$ is the vector connecting lattice sites r and r' . Since $G_{\uparrow\downarrow}(\mathbf{Q}, \mathbf{Q}')$ contains terms proportional to $\langle \Delta_{d,R}^\dagger \Delta_{d,R'} \rangle$ (where R and R' label plaquettes), a d -wave superfluid will exhibit interference fringes at $\mathbf{Q} + \mathbf{Q}' = 2\pi m \hat{\mathbf{z}}/a'$ for any integer (half-integer) m where $\hat{\mathbf{z}}$ is the unit vector along the stack when $\tilde{J}_\perp < 0$ (> 0). Since the state has $d_{x^2-y^2}$ symmetry, these fringes will be modulated in the x - y plane by an envelope that vanishes along the nodal lines $Q_x = \pm Q_y$ and $Q'_x = \pm Q'_y$ [37]. Therefore, the behavior of the fringes will be similar to that shown in Ref. [37], except that the superfluid phase will be signaled by fringes along $\hat{\mathbf{z}}$ instead of fringes in the x - y plane. Due to the absence of cycling transitions in molecules, the noise correlation measurements may have to be done by first converting the molecules back into atoms [12].

B. Two-dimensional realization of the perturbative regime

While we have discussed the one-dimensional stack of plaquettes, d -wave superfluidity is associated with a plane. An experiment observing d -wave superfluidity in a two-dimensional lattice would therefore be more relevant. The simple solution of increasing the spacing between plaquettes in a two-dimensional lattice to reduce the dipolar interactions is not feasible since this would typically reduce the tunneling amplitude t' between plaquettes to essentially zero.

However, if the energy difference between the rotor levels is not constant throughout a lattice of plaquettes, then the J_\perp dipolar interaction between plaquettes could be suppressed. This can be achieved by introducing an extra splitting Δ between rotor levels in some plaquettes and not in others. Then the Hamiltonian for each plaquette with the extra splitting gets an extra term

$$\Delta \sum_r S_r^z,$$

where the sum is taken over the four sites of the plaquette. Let (R_x, R_y) be the integer coordinates of the plaquette labeled by R . Suppose that the splitting is arranged in a checkerboard fashion, so, for integers n and m , plaquettes $(R_x + 2n, R_y + 2m)$ get the extra splitting Δ while plaquettes $(R_x + 2n + 1, R_y + 2m + 1)$ do not. In this case, dipolar interactions

between nearest-neighbor plaquettes will be suppressed by Δ since they are off resonant; however, dipolar interactions between next-nearest-neighbor (diagonal) plaquettes will not be suppressed since they will stay resonant. Thus, to make the perturbative calculations valid, four separate splittings would need to be introduced to suppress both nearest and next-nearest-neighbor interactions. However, with only one splitting Δ , a one-dimensional chain of plaquettes can be simulated experimentally.

Finally, for Δ that is large enough to make perturbation theory valid, a lattice of plaquettes filled with $|1,1\rangle$ and $|2,2\rangle$ states will typically be an excited state of the system of decoupled plaquettes, and the *d*-wave superfluid state will typically be an excited state of the full Hamiltonian of weakly coupled plaquettes. Nevertheless, such states can still be prepared adiabatically from appropriate excited states.

VI. CONCLUSIONS

We have shown that the t - J_{\perp} Hamiltonian on a square lattice, in the regime of weakly coupled plaquettes, exhibits a *d*-wave superfluid phase in addition to the checkerboard solid phase and phase separation. The addition of large J_z or W interactions destroys the superfluid phase; however, we have identified ranges of these parameters, for which the superfluid phase is enhanced. Any nonzero V destroys the superfluid phase in this perturbative analysis.

These perturbative calculations can be used as a qualitative guess for the behavior of the simplest experiments, which are outside of the perturbative limit. Furthermore, the perturbative regime can be accessed in experiments in a one-dimensional stack of plaquettes. The phase diagrams for the one-dimensional stack of plaquettes are qualitatively similar to the phase diagrams for the two-dimensional lattice of plaquettes. By experimentally observing the phase diagrams in both the perturbative and nonperturbative regimes for the one-dimensional stack, one may be able to understand the relationship between the calculations presented here and the nonperturbative phase diagrams. This knowledge may then be useful in understanding the relationship between the two-dimensional phase diagrams presented here and experiments on a homogeneous two-dimensional lattice. Similar results might be achievable experimentally with the large-magnetic-moment atoms dysprosium [67] and chromium [68] instead of polar molecules.

Ultracold polar molecules have the potential for experimentally observing *d*-wave superfluidity in a controlled environment that could allow us to learn about the physics of the t - J model. We hope that the insight gained by these investigations could help to explain the physics of high-temperature superconductivity and result in many theoretical and practical applications.

ACKNOWLEDGMENTS

We thank Maciej Lewenstein for suggesting the use of extra splittings between rotor levels to access the perturbative regime described in Sec. VB. We also thank John Preskill, Rajdeep Sensarma, Salvatore Manmana, Kaden Hazzard, Mikhail Lukin, Eugene Demler, Netanel Lindner, Norbert Schuch, Steven Flammia, Spyridon Michalakis, Gang Chen, Michael

Foss-Feig, and Xiao Yin for discussions. This work was supported by the Rose Hills Foundation, the Lee A. DuBridge Foundation, the NSF (PFC and Grants No. PHY-0803371 and PIF-0904017), and ARO with funding from the DARPA OLE program.

APPENDIX A: GROUP THEORETIC TECHNIQUES

In this Appendix, we describe the group theoretic techniques that we have used to diagonalize the single-plaquette Hamiltonians and to study their symmetries. Exact diagonalization [47] is discussed in general in Appendix A1, while the symmetries [33,38] of the irreducible representations of D_4 are discussed in Appendix A2. Finally, in Appendix A3, we use symmetry arguments to explain why the overall scale of the phase diagrams in the stack geometry is larger than the corresponding scale in the two-dimensional geometry. Related group theoretic techniques are discussed in the context of exact diagonalization of the Hubbard Hamiltonian in Refs. [69,70].

1. Diagonalization of the Hamiltonian

As is discussed in Sec. III A, the operators n_{\uparrow} and n_{\downarrow} commute with the Hamiltonian Eq. (1) and with each other, so we diagonalize subspaces with fixed values of n_{\uparrow} and n_{\downarrow} separately. The Hamiltonian Eq. (1) has the symmetries of a square described by the group D_4 so we use the irreducible representations of D_4 to further simplify the task of diagonalizing each subspace. The discussion below uses D_4 as an example but is general and can be applied to any finite group. In this section, we closely follow Ref. [47].

D_4 has $h = 8$ group elements corresponding to the symmetries of a square, considered here to be lying in the x - y plane: the identity E , rotations by π around the x , y , and z axes C_{2x} , C_{2y} , and C_{2z} , rotations by π around the lines $x = y$ and $x = -y$ C_{2xy} and $C_{2x\bar{y}}$, and counterclockwise and clockwise rotations by $\pi/2$ around the z axis C_{4z} and C_{4z}^{-1} . There are five conjugacy classes and thus five irreducible representations for D_4 . The five classes are the identity E , the π rotation about the z axis C_2 consisting of C_{2z} , the two $\pi/2$ rotations $2C_4$ consisting of C_{4z} and C_{4z}^{-1} , the two π rotations about the x and y axes $2C'_2$ consisting of C_{2x} and C_{2y} , and the two π rotations about the lines $x = y$ and $x = -y$ $2C''_2$ consisting of C_{2xy} and $C_{2x\bar{y}}$. There are four one-dimensional irreducible representations A_1 , A_2 , B_1 , and B_2 and one two-dimensional irreducible representation E . The character table for D_4 is shown in Table III.

TABLE III. Character table for the group D_4 taken from Ref. [47], along with the classification of each irreducible representation as is discussed in Appendix A2.

	E	C_2	$2C_4$	$2C'_2$	$2C''_2$	Symmetries
A_1	1	1	1	1	1	s
A_2	1	1	1	-1	-1	s
B_1	1	1	-1	1	-1	$d_{x^2-y^2}$
B_2	1	1	-1	-1	1	d_{xy}
E	2	-2	0	0	0	p_x and p_y

TABLE IV. Group structure of the single-plaquette Hilbert space with D_4 symmetry in the presence of n_\uparrow and n_\downarrow conservation. The results are symmetric on interchange of n_\uparrow and n_\downarrow .

n_\uparrow, n_\downarrow	Dimension	Representation
1,0	4	$A_1 \oplus B_2 \oplus E$
2,0	6	$A_2 \oplus B_2 \oplus 2E$
1,1	12	$2A_1 \oplus A_2 \oplus B_1 \oplus 2B_2 \oplus 3E$
3,0	4	$A_2 \oplus B_1 \oplus E$
2,1	12	$A_1 \oplus 2A_2 \oplus 2B_1 \oplus B_2 \oplus 3E$
4,0	1	B_1
3,1	4	$A_2 \oplus B_1 \oplus E$
2,2	6	$A_1 \oplus A_2 \oplus 2B_1 \oplus E$

The number of times the n th irreducible representation appears in the decomposition of a reducible representation is [47]

$$a_n = \frac{1}{h} \sum_R \chi^{(n)}(R)^* \chi(R), \quad (\text{A1})$$

where the sum is taken over all group elements R , $\chi^{(n)}(R)$ is the character of R in the n th irreducible representation, and $\chi(R)$ is the character of R in the reducible representation. Let $|\alpha\rangle$ denote a basis function in the occupation basis. By writing the eight symmetry operations in the occupation basis for a fixed n_\uparrow and n_\downarrow subspace of the full Hilbert space, we calculate the character of each element in this occupation representation. Using Eq. (A1), we calculate the group structure of each of these subspaces. The results are shown in Table IV.

As we will see below, the Hamiltonian is block diagonal in the representation basis, so we would like to change basis from the occupation basis $|\alpha\rangle$ to the representation basis $|\phi_{i\lambda}^{(n)}\rangle$ to reduce the dimensions of the matrices needing to be diagonalized. Here $|\phi_{i\lambda}^{(n)}\rangle$ refers to a normalized basis function for the i th row of the n th irreducible representation. If the n th irreducible representation is present more than once in the decomposition of the occupation representation, then there will be $a_n > 1$ orthogonal basis functions for the same row of the n th irreducible representation indexed by λ . Let there be c irreducible representations and c classes. (For D_4 , $c = 5$.) $|\alpha\rangle$ can be expanded in terms of the $|\phi_{i\lambda}^{(n)}\rangle$ as

$$|\alpha\rangle = \sum_{n=1}^c \sum_{i=1}^{l_n} \sum_{\lambda=1}^{a_n} b_{i\lambda}^{(n)} |\phi_{i\lambda}^{(n)}\rangle, \quad (\text{A2})$$

where l_n is the dimension of the n th irreducible representation.

The $|\phi_{i\lambda}^{(n)}\rangle$ and $b_{i\lambda}^{(n)}$ are found by applying the projection operator

$$P_{ij}^{(n)} = \frac{l_n}{h} \sum_R \Gamma^{(n)}(R)_{ij}^* P_R \quad (\text{A3})$$

to $|\alpha\rangle$. $\Gamma^{(n)}(R)$ is the n th irreducible representation of the group element R , and P_R is the operator corresponding to R that acts on functions instead of coordinates and satisfies

$$P_R g(x) = g(R^{-1}x).$$

To compute P_R in practice, one finds the action of R on the spatial indices of the creation operators used to define the second-quantized wave function.

The projector $P_{ii}^{(n)}$ projects into the i th row of the n th irreducible representation, so

$$|f_{i\lambda(\alpha)}^{(n)}\rangle = P_{ii}^{(n)} |\alpha\rangle \quad (\text{A4})$$

yields a function $|f_{i\lambda(\alpha)}^{(n)}\rangle$ that transforms as the i th row of the n th irreducible representation. For the i th row of the n th irreducible representation, a given $|\alpha\rangle$ will only be composed of a function belonging to one of the a_n copies, the $\lambda(\alpha)$ th copy, of the i th row of the n th irreducible representation even if $a_n > 1$. Note that $|f_{i\lambda(\alpha)}^{(n)}\rangle$ will be zero if $a_n = 0$. For each nonzero $|f_{i\lambda(\alpha)}^{(n)}\rangle$, the corresponding normalized basis function is, up to a global phase,

$$|\phi_{i\lambda(\alpha)}^{(n)}\rangle = (|f_{i\lambda(\alpha)}^{(n)}\rangle |f_{i\lambda(\alpha)}^{(n)}\rangle)^{-1/2} |f_{i\lambda(\alpha)}^{(n)}\rangle.$$

The coefficients $b_{i\lambda}^{(n)}$ of the decomposition Eq. (A2) are

$$b_{i\lambda}^{(n)} = \begin{cases} 0 & \text{if } a_n = 0 \\ (|f_{i\lambda(\alpha)}^{(n)}\rangle |f_{i\lambda(\alpha)}^{(n)}\rangle)^{1/2} \delta_{\lambda,\lambda(\alpha)} & \text{if } a_n \neq 0 \end{cases}.$$

To find all of the basis functions for the representation basis, we compute Eq. (A4) for every basis function $|\alpha\rangle$ in the occupation basis for all $P_{ii}^{(n)}$.¹ By applying the same projection operator to different functions $|\alpha\rangle$, different functions for the same row of the same representation will be generated for all $\lambda = 1, \dots, a_n$. Once all of the $|\phi_{i\lambda}^{(n)}\rangle$ have been found, the Hamiltonian can be transformed into the representation basis by

$$H_{\text{representation}} = S^\dagger H_{\text{occupation}} S,$$

where S is the transformation matrix given by $S_{\alpha,\phi} = \langle \alpha | \phi_{i\lambda}^{(n)} \rangle$. Since P_R commutes with H for all R ,

$$\begin{aligned} \langle \phi_{i\lambda(\alpha)}^{(n)} | H | \phi_{j\mu(\beta)}^{(m)} \rangle &\propto \langle \alpha | P_{ii}^{(n)} H P_{jj}^{(m)} | \beta \rangle \\ &= \langle \alpha | H P_{ii}^{(n)} P_{jj}^{(m)} | \beta \rangle \propto \delta_{n,m} \delta_{i,j}. \end{aligned}$$

Thus, matrix elements between different irreducible representations or different rows within the same irreducible representation vanish. Therefore, this transformation into the representation basis can be made separately for each row of each irreducible representation, and each of the resulting Hamiltonians can be diagonalized separately. This greatly reduces the dimension of the Hamiltonians that need to be diagonalized since the dimension of the Hamiltonian for the i th row of the n th irreducible representation is a_n . States found in the representation basis can be transformed back into the occupation basis by

$$|\alpha\rangle |\psi\rangle = \sum_{\phi} S_{\alpha,\phi} \langle \phi | \psi \rangle.$$

¹If $l_n > 1$, once the basis function for a single row, the i th row, of the n th irreducible representation has been found by Eq. (A4), it is also possible to find the basis functions for the other $l_n - 1$ rows by applying the projection operator to the basis function just found by the property $|\phi_{j\lambda}^{(n)}\rangle = P_{ji}^{(n)} |\phi_{i\lambda}^{(n)}\rangle$.

In order to compute the projector Eq. (A3), it is necessary to know the representation $\Gamma^{(n)}(R)$ of each group element R in each representation n . For the one-dimensional representations, the representations $\Gamma^{(n)}(R)$ are just the characters $\chi^{(n)}(R)$ listed in Table III. In the (x, y) basis, the representations of the group elements in the E representation are

$$\begin{aligned} \Gamma^{(E)}(E) &= \begin{bmatrix} 1 & 0 \\ 0 & 1 \end{bmatrix} & \Gamma^{(E)}(C_{2z}) &= \begin{bmatrix} -1 & 0 \\ 0 & -1 \end{bmatrix} \\ \Gamma^{(E)}(C_{4z}) &= \begin{bmatrix} 0 & -1 \\ 1 & 0 \end{bmatrix} & \Gamma^{(E)}(C_{4z}^{-1}) &= \begin{bmatrix} 0 & 1 \\ -1 & 0 \end{bmatrix} \\ \Gamma^{(E)}(C_{2x}) &= \begin{bmatrix} 1 & 0 \\ 0 & -1 \end{bmatrix} & \Gamma^{(E)}(C_{2y}) &= \begin{bmatrix} -1 & 0 \\ 0 & 1 \end{bmatrix} \\ \Gamma^{(E)}(C_{2xy}) &= \begin{bmatrix} 0 & 1 \\ 1 & 0 \end{bmatrix} & \Gamma^{(E)}(C_{2x\bar{y}}) &= \begin{bmatrix} 0 & -1 \\ -1 & 0 \end{bmatrix}. \end{aligned} \quad (\text{A5})$$

2. Classification of the eigenstates

In this section, we classify the symmetries of the five representations of D_4 and give examples of states transforming as each of these representations. Since the A and B representations are one dimensional, we can study their symmetries directly from the character table (Table III). The A states are symmetric under $\pi/2$ rotations $2C_4$, while the B states are antisymmetric under these rotations. For this reason, the A states are classified as s wave and the B states are classified as d wave. The A_1 representation is symmetric under all five classes, while the A_2 representation is antisymmetric under $2C_2'$ and $2C_2''$. The B_1 representation is symmetric under $2C_2'$ and is antisymmetric under $2C_2''$, while the B_2 representation is antisymmetric under $2C_2'$ and is symmetric under $2C_2''$. Thus, B_1 is classified as $d_{x^2-y^2}$ and B_2 is classified as d_{xy} .

The E representation is two dimensional, so we need to consider the representations of the group elements given by Eq. (A5). Both rows of the representation are antisymmetric under π rotations about the z axis. For this reason, E is classified as p wave. The first row transforms into the second row and the second row transforms into negative the first row under a positive rotation by $\pi/2$ about the z axis. The first row is antisymmetric and the second row is symmetric under a π rotation about the x axis. The first row transforms into the second row and the second row transforms into the first row under a π rotation about the line $y = x$. Similar considerations for the other rotations lead to the classification of the first row of the E representation as p_x and the second row as p_y .

Simple examples of states in the A_1 , B_2 , and E representations come from $n_\uparrow = 1$ and $n_\downarrow = 0$. An example of an A_1 state is

$$|A_1\rangle = \frac{1}{2} (|\uparrow 000\rangle + |0 \uparrow 00\rangle + |00 \uparrow 0\rangle + |000 \uparrow\rangle).$$

We use the notation in which, for example,

$$|\uparrow 0 \downarrow 0\rangle = c_{1\uparrow}^\dagger c_{3\downarrow}^\dagger |0\rangle,$$

and the numbering of sites within a plaquette is given in Fig. 1. This state is clearly invariant under all five of the D_4 classes. An example of a B_2 state is

$$|B_2\rangle = \frac{1}{2} (|\uparrow 000\rangle - |0 \uparrow 00\rangle + |00 \uparrow 0\rangle - |000 \uparrow\rangle).$$

This state is invariant under C_2 and $2C_2'$ but changes sign under $2C_4$ and $2C_4'$. An example of two E states is

$$\begin{aligned} |E_x\rangle &= \frac{1}{2} (|\uparrow 000\rangle - |0 \uparrow 00\rangle - |00 \uparrow 0\rangle + |000 \uparrow\rangle), \\ |E_y\rangle &= \frac{1}{2} (|\uparrow 000\rangle + |0 \uparrow 00\rangle - |00 \uparrow 0\rangle - |000 \uparrow\rangle). \end{aligned}$$

These states are antisymmetric under π rotations about z . Under a positive rotation by $\pi/2$ about z , $|E_x\rangle \rightarrow |E_y\rangle$ and $|E_y\rangle \rightarrow -|E_x\rangle$. Under a π rotation about the x axis, $|E_x\rangle \rightarrow |E_y\rangle$ and $|E_y\rangle \rightarrow -|E_x\rangle$. Under a π rotation about the line $y = x$, $|E_x\rangle \rightarrow |E_y\rangle$ and $|E_y\rangle \rightarrow |E_x\rangle$. Thus, $|E_x\rangle$ transforms as p_x and $|E_y\rangle$ transforms as p_y .

A simple example of an A_2 state comes from $n_\uparrow = 2$ and $n_\downarrow = 0$, where

$$\begin{aligned} |A_2\rangle &= \frac{1}{2} (|\uparrow\uparrow 00\rangle + |0 \uparrow\uparrow 0\rangle + |00 \uparrow\uparrow\rangle - |\uparrow 00 \uparrow\rangle) \\ &= \frac{1}{2} (c_{1\uparrow}^\dagger c_{2\uparrow}^\dagger + c_{2\uparrow}^\dagger c_{3\uparrow}^\dagger + c_{3\uparrow}^\dagger c_{4\uparrow}^\dagger + c_{4\uparrow}^\dagger c_{1\uparrow}^\dagger) |0\rangle. \end{aligned}$$

This state is invariant under C_2 and $2C_4$ since these transformations cyclically permute the indices. Under $2C_2'$ and $2C_2''$, $|A_2\rangle \rightarrow -|A_2\rangle$ since this corresponds to swapping indices.

A simple example of a B_1 state is just the state from $n_\uparrow = 4$ and $n_\downarrow = 0$

$$|B_1\rangle = |\uparrow\uparrow\uparrow\uparrow\rangle = c_{1\uparrow}^\dagger c_{2\uparrow}^\dagger c_{3\uparrow}^\dagger c_{4\uparrow}^\dagger |0\rangle.$$

As can be seen by appropriately switching the indicies on the creation operators, this state has the B_1 symmetries discussed above.

3. Scale increase in the phase diagrams for the stack geometry

In this section, we use symmetry arguments to explain the increase in the overall scale of phase diagrams for the stack geometry (Figs. 10–12) relative to the corresponding diagrams for the two-dimensional geometry (Figs. 3, 7, and 8). The main reason for this increase is that the J'_\perp , J''_\perp , and W' transition matrix elements between the low- and high-energy subspaces decrease as J''/J' and J'''/J' are varied from 0 to 1. As a result, all phase transitions occur at smaller values of t' . To gain intuition for why these matrix elements decrease as J'' and J''' approach J' , we study the t - J_\perp Hamiltonian for the stack geometry in the regime where $J'_\perp = J''_\perp = J'''_\perp$ (obtained as $a'/a \rightarrow \infty$). A similar argument holds for the other Hamiltonians considered.

Consider two neighboring plaquettes in a stack in the $|2,2\rangle|2,2\rangle$ state coupled by the J'_\perp perturbing Hamiltonian $H_{1\perp}$ with $J'_\perp = J''_\perp = J'''_\perp$. From Table II, both plaquettes have B_1 symmetry. Since every vertex in one of the plaquettes is equally coupled to every vertex in the other plaquette, $H_{1\perp}$ is symmetric under arbitrary permutations of the vertices within one of the plaquettes. As a result, the matrix element

$$\langle 1,3 | \langle 3,1 | H_{1\perp} | 2,2 \rangle | 2,2 \rangle$$

will vanish unless both $|1,3\rangle$ and $|3,1\rangle$ have B_1 symmetry; otherwise, an appropriate permutation can be used to show that this matrix element is equal to negative itself. This drastically reduces the magnitude of $f_\perp^{(4,4)}$ relative to its value in the $J''_\perp = J'''_\perp = 0$ case. A similar argument shows that $f_\perp^{(4,2)}$ and $f_\perp^{(2,2)}$ vanish for $J'_\perp = J''_\perp = J'''_\perp$ (since the $|1,3\rangle$ and $|3,1\rangle$ manifolds have no A_1 states. See Table IV).

APPENDIX B: BASIS VECTORS IN THE REPRESENTATION BASIS

In this Appendix, we list the basis vectors for the irreducible representations for D_4 . The results are symmetric on interchange of up spins with down spins. We use the notation $|n_\uparrow, n_\downarrow(\Gamma)\rangle$ to refer to the basis vector for a plaquette with n_\uparrow up spins and n_\downarrow down spins in the irreducible representation Γ . If there are $a_n > 1$ copies of an irreducible representation, we denote them by a superscript. We use subscripts x and y to denote the first and second rows of the E representation, respectively. Thus $|1, 1(E_y^1)\rangle$ refers to the basis vector for $|1, 1\rangle$ in the first copy of the second row of the E representation, and $|2, 1(B_1^2)\rangle$ refers to the basis vector for $|2, 1\rangle$ in the second copy of the B_1 representation.

1. $n_\uparrow = 1$ and $n_\downarrow = 0$

$$|1, 0(A_1)\rangle = \frac{1}{2}(|\uparrow 000\rangle + |0 \uparrow 00\rangle + |00 \uparrow 0\rangle + |000 \uparrow\rangle)$$

$$|1, 0(B_2)\rangle = \frac{1}{2}(|\uparrow 000\rangle - |0 \uparrow 00\rangle + |00 \uparrow 0\rangle - |000 \uparrow\rangle)$$

$$|1, 0(E_x)\rangle = \frac{1}{2}(|\uparrow 000\rangle - |0 \uparrow 00\rangle - |00 \uparrow 0\rangle + |000 \uparrow\rangle)$$

$$|1, 0(E_y)\rangle = \frac{1}{2}(|\uparrow 000\rangle + |0 \uparrow 00\rangle - |00 \uparrow 0\rangle - |000 \uparrow\rangle)$$

2. $n_\uparrow = 2$ and $n_\downarrow = 0$

$$|2, 0(A_2)\rangle = \frac{1}{2}(|\uparrow \uparrow 00\rangle + |0 \uparrow \uparrow 0\rangle - |\uparrow \uparrow 00\rangle + |00 \uparrow \uparrow\rangle)$$

$$|2, 0(B_2)\rangle = \frac{1}{2}(|\uparrow \uparrow 00\rangle - |0 \uparrow \uparrow 0\rangle + |\uparrow \uparrow 00\rangle + |00 \uparrow \uparrow\rangle)$$

$$|2, 0(E_x^1)\rangle = \frac{1}{\sqrt{2}}(|\uparrow \uparrow 00\rangle - |00 \uparrow \uparrow\rangle)$$

$$|2, 0(E_y^1)\rangle = \frac{1}{\sqrt{2}}(|0 \uparrow \uparrow 0\rangle + |\uparrow \uparrow 00\rangle)$$

$$|2, 0(E_x^2)\rangle = \frac{1}{\sqrt{2}}(|\uparrow \uparrow 00\rangle - |0 \uparrow \uparrow 0\rangle)$$

$$|2, 0(E_y^2)\rangle = \frac{1}{\sqrt{2}}(|\uparrow \uparrow 00\rangle + |0 \uparrow \uparrow 0\rangle)$$

3. $n_\uparrow = 1$ and $n_\downarrow = 1$

$$|1, 1(A_1^1)\rangle = \frac{1}{2\sqrt{2}}(|\downarrow \uparrow 00\rangle - |\uparrow \downarrow 00\rangle + |0 \downarrow \uparrow 0\rangle - |0 \uparrow \downarrow 0\rangle + |\downarrow 0 \uparrow 0\rangle + |00 \downarrow \uparrow\rangle - |\uparrow 00 \downarrow\rangle - |00 \uparrow \downarrow\rangle)$$

$$|1, 1(A_1^2)\rangle = \frac{1}{2}(|\downarrow 0 \uparrow 0\rangle - |\uparrow 0 \downarrow 0\rangle + |0 \downarrow 0 \uparrow\rangle - |0 \uparrow 0 \downarrow\rangle)$$

$$|1, 1(A_2)\rangle = \frac{1}{2\sqrt{2}}(|\downarrow \uparrow 00\rangle + |\uparrow \downarrow 00\rangle + |0 \downarrow \uparrow 0\rangle + |0 \uparrow \downarrow 0\rangle - |\downarrow 0 \uparrow 0\rangle + |00 \downarrow \uparrow\rangle - |\uparrow 00 \downarrow\rangle + |00 \uparrow \downarrow\rangle)$$

$$|1, 1(B_1)\rangle = \frac{1}{2\sqrt{2}}(|\downarrow \uparrow 00\rangle - |\uparrow \downarrow 00\rangle - |0 \downarrow \uparrow 0\rangle + |0 \uparrow \downarrow 0\rangle - |\downarrow 0 \uparrow 0\rangle + |00 \downarrow \uparrow\rangle + |\uparrow 00 \downarrow\rangle - |00 \uparrow \downarrow\rangle)$$

$$|1, 1(B_2^1)\rangle = \frac{1}{2\sqrt{2}}(|\downarrow \uparrow 00\rangle + |\uparrow \downarrow 00\rangle - |0 \downarrow \uparrow 0\rangle - |0 \uparrow \downarrow 0\rangle + |\downarrow 0 \uparrow 0\rangle + |00 \downarrow \uparrow\rangle + |\uparrow 00 \downarrow\rangle + |00 \uparrow \downarrow\rangle)$$

$$|1, 1(B_2^2)\rangle = \frac{1}{2}(|\downarrow 0 \uparrow 0\rangle - |\uparrow 0 \downarrow 0\rangle - |0 \downarrow 0 \uparrow\rangle + |0 \uparrow 0 \downarrow\rangle)$$

$$|1, 1(E_x^1)\rangle = \frac{1}{2}(|\downarrow \uparrow 00\rangle + |\uparrow \downarrow 00\rangle - |00 \downarrow \uparrow\rangle - |00 \uparrow \downarrow\rangle)$$

$$|1, 1(E_y^1)\rangle = \frac{1}{2}(|0 \uparrow \downarrow 0\rangle + |0 \downarrow \uparrow 0\rangle + |\uparrow 00 \downarrow\rangle + |\downarrow 00 \uparrow\rangle)$$

$$|1, 1(E_x^2)\rangle = \frac{1}{2}(|0 \uparrow \downarrow 0\rangle - |0 \downarrow \uparrow 0\rangle - |\uparrow 00 \downarrow\rangle + |\downarrow 00 \uparrow\rangle)$$

$$|1, 1(E_y^2)\rangle = \frac{1}{2}(|\downarrow \uparrow 00\rangle - |\uparrow \downarrow 00\rangle - |00 \downarrow \uparrow\rangle + |00 \uparrow \downarrow\rangle)$$

$$|1, 1(E_x^3)\rangle = \frac{1}{2}(|\downarrow 0 \uparrow 0\rangle + |\uparrow 0 \downarrow 0\rangle - |0 \downarrow 0 \uparrow\rangle - |0 \uparrow 0 \downarrow\rangle)$$

$$|1, 1(E_y^3)\rangle = \frac{1}{2}(|\downarrow 0 \uparrow 0\rangle + |\uparrow 0 \downarrow 0\rangle + |0 \downarrow 0 \uparrow\rangle + |0 \uparrow 0 \downarrow\rangle)$$

4. $n_\uparrow = 3$ and $n_\downarrow = 0$

$$|3, 0(A_2)\rangle = \frac{1}{2}(|\uparrow \uparrow \uparrow 0\rangle + |\uparrow \uparrow 0 \uparrow\rangle + |\uparrow 0 \uparrow \uparrow\rangle + |0 \uparrow \uparrow \uparrow\rangle)$$

$$|3, 0(B_1)\rangle = \frac{1}{2}(|\uparrow \uparrow \uparrow 0\rangle - |\uparrow \uparrow 0 \uparrow\rangle + |\uparrow 0 \uparrow \uparrow\rangle - |0 \uparrow \uparrow \uparrow\rangle)$$

$$|3, 0(E_x)\rangle = \frac{1}{2}(|\uparrow \uparrow \uparrow 0\rangle + |\uparrow \uparrow 0 \uparrow\rangle - |\uparrow 0 \uparrow \uparrow\rangle - |0 \uparrow \uparrow \uparrow\rangle)$$

$$|3, 0(E_y)\rangle = \frac{1}{2}(|\uparrow \uparrow \uparrow 0\rangle - |\uparrow \uparrow 0 \uparrow\rangle - |\uparrow 0 \uparrow \uparrow\rangle + |0 \uparrow \uparrow \uparrow\rangle)$$

5. $n_\uparrow = 2$ and $n_\downarrow = 1$

$$|2, 1(A_1)\rangle = \frac{1}{2\sqrt{2}}(|\downarrow \uparrow \uparrow 0\rangle - |\uparrow \uparrow \downarrow 0\rangle - |\uparrow \downarrow \uparrow 0\rangle - |\downarrow 0 \uparrow \uparrow\rangle + |0 \downarrow \uparrow \uparrow\rangle + |\uparrow 0 \downarrow \uparrow\rangle + |\uparrow \uparrow 0 \downarrow\rangle - |0 \uparrow \uparrow \downarrow\rangle)$$

$$|2, 1(A_2^1)\rangle = \frac{1}{2\sqrt{2}}(|\downarrow \uparrow \uparrow 0\rangle + |\uparrow \uparrow \downarrow 0\rangle + |\uparrow \downarrow \uparrow 0\rangle + |\downarrow 0 \uparrow \uparrow\rangle + |0 \downarrow \uparrow \uparrow\rangle + |\uparrow 0 \downarrow \uparrow\rangle + |\uparrow \uparrow 0 \downarrow\rangle + |0 \uparrow \uparrow \downarrow\rangle)$$

$$|2, 1(A_2^2)\rangle = \frac{1}{2}(|\uparrow \downarrow \uparrow 0\rangle + |\downarrow \uparrow 0 \uparrow\rangle + |0 \uparrow \downarrow \uparrow\rangle + |\uparrow 0 \uparrow \downarrow\rangle)$$

$$|2, 1(B_1^1)\rangle = \frac{1}{2\sqrt{2}}(|\downarrow \uparrow \uparrow 0\rangle + |\uparrow \uparrow \downarrow 0\rangle - |\uparrow \downarrow \uparrow 0\rangle + |\downarrow 0 \uparrow \uparrow\rangle - |0 \downarrow \uparrow \uparrow\rangle + |\uparrow 0 \downarrow \uparrow\rangle - |\uparrow \uparrow 0 \downarrow\rangle - |0 \uparrow \uparrow \downarrow\rangle)$$

$$|2, 1(B_1^2)\rangle = \frac{1}{2}(|\uparrow \downarrow \uparrow 0\rangle - |\downarrow \uparrow 0 \uparrow\rangle - |0 \uparrow \downarrow \uparrow\rangle + |\uparrow 0 \uparrow \downarrow\rangle)$$

$$|2, 1(B_2)\rangle = \frac{1}{2\sqrt{2}}(|\downarrow \uparrow \uparrow 0\rangle - |\uparrow \uparrow \downarrow 0\rangle + |\uparrow \downarrow \uparrow 0\rangle - |\downarrow 0 \uparrow \uparrow\rangle - |0 \downarrow \uparrow \uparrow\rangle + |\uparrow 0 \downarrow \uparrow\rangle - |\uparrow \uparrow 0 \downarrow\rangle + |0 \uparrow \uparrow \downarrow\rangle)$$

$$|2, 1(E_x^1)\rangle = \frac{1}{2}(|\downarrow \uparrow \uparrow 0\rangle + |\uparrow \downarrow \uparrow 0\rangle - |\uparrow 0 \downarrow \uparrow\rangle - |0 \uparrow \uparrow \downarrow\rangle)$$

$$|2, 1(E_y^1)\rangle = \frac{1}{2}(|\uparrow \uparrow \downarrow 0\rangle - |\downarrow 0 \uparrow \uparrow\rangle + |0 \downarrow \uparrow \uparrow\rangle - |\uparrow \uparrow 0 \downarrow\rangle)$$

$$\begin{aligned}
 |2,1(E_x^2)\rangle &= \frac{1}{2}(|\uparrow\uparrow\downarrow 0\rangle - |\downarrow 0\uparrow\uparrow\rangle - |0\downarrow\uparrow\uparrow\rangle + |\uparrow\uparrow 0\downarrow\rangle) \\
 |2,1(E_y^2)\rangle &= \frac{1}{2}(|\downarrow\uparrow\uparrow 0\rangle - |\uparrow\downarrow 0\uparrow\rangle - |\uparrow 0\downarrow\uparrow\rangle + |0\uparrow\uparrow\downarrow\rangle) \\
 |2,1(E_x^3)\rangle &= \frac{1}{2}(|\uparrow\downarrow\uparrow 0\rangle + |\downarrow\uparrow 0\uparrow\rangle - |0\uparrow\downarrow\uparrow\rangle - |\uparrow 0\uparrow\downarrow\rangle) \\
 |2,1(E_y^3)\rangle &= \frac{1}{2}(|\uparrow\downarrow\uparrow 0\rangle - |\downarrow\uparrow 0\uparrow\rangle + |0\uparrow\downarrow\uparrow\rangle - |\uparrow 0\uparrow\downarrow\rangle)
 \end{aligned}$$

6. $n_\uparrow = 4$ and $n_\downarrow = 0$

$$|4,0(B_1)\rangle = |\uparrow\uparrow\uparrow\uparrow\rangle$$

7. $n_\uparrow = 3$ and $n_\downarrow = 1$

$$\begin{aligned}
 |3,1(A_2)\rangle &= \frac{1}{2}(|\downarrow\uparrow\uparrow\uparrow\rangle - |\uparrow\downarrow\uparrow\uparrow\rangle + |\uparrow\uparrow\downarrow\uparrow\rangle - |\uparrow\uparrow\uparrow\downarrow\rangle) \\
 |3,1(B_1)\rangle &= \frac{1}{2}(|\downarrow\uparrow\uparrow\uparrow\rangle + |\uparrow\downarrow\uparrow\uparrow\rangle + |\uparrow\uparrow\downarrow\uparrow\rangle + |\uparrow\uparrow\uparrow\downarrow\rangle) \\
 |3,1(E_x)\rangle &= \frac{1}{2}(|\downarrow\uparrow\uparrow\uparrow\rangle - |\uparrow\downarrow\uparrow\uparrow\rangle - |\uparrow\uparrow\downarrow\uparrow\rangle + |\uparrow\uparrow\uparrow\downarrow\rangle) \\
 |3,1(E_y)\rangle &= -\frac{1}{2}(|\downarrow\uparrow\uparrow\uparrow\rangle + |\uparrow\downarrow\uparrow\uparrow\rangle - |\uparrow\uparrow\downarrow\uparrow\rangle - |\uparrow\uparrow\uparrow\downarrow\rangle)
 \end{aligned}$$

8. $n_\uparrow = 2$ and $n_\downarrow = 2$

$$\begin{aligned}
 |2,2(A_1)\rangle &= \frac{1}{2}(|\downarrow\downarrow\uparrow\uparrow\rangle - |\uparrow\downarrow\downarrow\uparrow\rangle - |\downarrow\uparrow\downarrow\uparrow\rangle + |\uparrow\uparrow\downarrow\downarrow\rangle) \\
 |2,2(A_2)\rangle &= \frac{1}{\sqrt{2}}(|\downarrow\downarrow\downarrow\uparrow\rangle - |\uparrow\downarrow\downarrow\downarrow\rangle) \\
 |2,2(B_1^1)\rangle &= \frac{1}{2}(|\downarrow\downarrow\uparrow\uparrow\rangle + |\uparrow\downarrow\downarrow\uparrow\rangle + |\downarrow\uparrow\downarrow\uparrow\rangle + |\uparrow\uparrow\downarrow\downarrow\rangle) \\
 |2,2(B_1^2)\rangle &= \frac{1}{\sqrt{2}}(|\downarrow\downarrow\downarrow\uparrow\rangle + |\uparrow\downarrow\downarrow\downarrow\rangle) \\
 |2,2(E_x)\rangle &= \frac{1}{\sqrt{2}}(|\uparrow\downarrow\downarrow\uparrow\rangle - |\downarrow\uparrow\downarrow\downarrow\rangle) \\
 |2,2(E_y)\rangle &= \frac{1}{\sqrt{2}}(|\downarrow\downarrow\uparrow\uparrow\rangle - |\uparrow\uparrow\downarrow\downarrow\rangle)
 \end{aligned}$$

APPENDIX C: EXPLICIT EXPRESSIONS FOR IMPORTANT GROUND STATES AND ENERGIES

In this Appendix, we give explicit expressions for the ground states and energies for those $|2\rangle$ and $|4\rangle$ states responsible for *d*-wave superfluidity in the t - J_\perp Hamiltonian, the t - J_\perp - J_z Hamiltonian, and the t - J - W Hamiltonian with $J_\perp = J_z = J$. We also discuss intuition for the symmetries of some of these states.

1. t - J_\perp Hamiltonian

Here we give the $|2\rangle$ and $|4\rangle$ ground states of the t - J_\perp Hamiltonian responsible for *d*-wave superfluidity (see Table II and Fig. 2). The *s*-wave symmetric $|1,1\rangle$ ground state for $J_\perp/t > -1.22$ is

$$|1,1(A_1)\rangle \propto b|1,1(A_1^1)\rangle + |1,1(A_1^2)\rangle \quad (C1)$$

with energy

$$\begin{aligned}
 E_g(1,1) &= -\frac{1}{16} \left[\sqrt{(18 - 8\sqrt{2}) \left(\frac{J_\perp}{t}\right)^2 + 2048} \right. \\
 &\quad \left. + (4 + \sqrt{2}) \frac{J_\perp}{t} \right], \quad (C2)
 \end{aligned}$$

where

$$b = \frac{1}{32} \left[\sqrt{(9 - 4\sqrt{2}) \left(\frac{J_\perp}{t}\right)^2 + 1024} + (2\sqrt{2} - 1) \frac{J_\perp}{t} \right].$$

The *d*-wave symmetric $|2,2\rangle$ ground state for $J_\perp/t > 0$ is

$$|2,2(B_1)\rangle \propto \frac{\sqrt{65} - 1}{8} |2,2(B_1^1)\rangle - |2,2(B_1^2)\rangle \quad (C3)$$

with energy

$$E_g(2,2) = \frac{1 - \sqrt{65} J_\perp}{4\sqrt{2} t}.$$

We can understand the symmetries of the $|2\rangle$ ground states as follows. In the limit of vanishing t , the ground state will be an eigenstate of the J_\perp interaction. The two eigenstates of the J_\perp interaction for an up and a down molecule on sites r and r' are

$$|\pm\rangle_{rr'} = \frac{1}{\sqrt{2}} (c_{r\uparrow}^\dagger c_{r'\downarrow}^\dagger \pm c_{r\downarrow}^\dagger c_{r'\uparrow}^\dagger) |0\rangle \quad (C4)$$

since

$$\frac{J_\perp}{2} (S_r^+ S_{r'}^- + S_r^- S_{r'}^+) |\pm\rangle_{rr'} = \pm \frac{J_\perp}{2} |\pm\rangle_{rr'}.$$

[Note that $|- \rangle_{rr'} = s_{rr'}^\dagger |0\rangle$ where $s_{rr'}^\dagger$ is given by Eq. (4)]. Thus for positive J_\perp , the singlet state $|- \rangle$ is the ground state of the J_\perp interaction. Note that it is disadvantageous to have identical spins since, in that case, the J_\perp interaction vanishes. For two molecules with small tunneling amplitude t , the $|2\rangle$ ground state is thus a superposition of singlets on the four nearest-neighbor bonds. Diagonalizing the effective Hamiltonian of this system shows that the ground state is the following symmetric superposition:

$$|- \rangle_{12} + |- \rangle_{23} + |- \rangle_{34} + |- \rangle_{41}.$$

This state has *s*-wave symmetry and is proportional to the basis vector $|1,1(A_1)\rangle$, consistent with Eq. (C1). For negative J_\perp , the $|+\rangle$ state is the ground state of the J_\perp interaction on two sites, and the two resulting single-plaquette ground states have *p*-wave symmetry.

The symmetries of the $|4\rangle$ ground states can be understood by considering only nearest-neighbor interactions. In this case, for positive J_\perp , the ground state is

$$|2,2(B_1^2)\rangle - |2,2(B_1^1)\rangle,$$

which has $d_{x^2-y^2}$ symmetry. For negative J_\perp , the ground state is

$$|2,2(B_1^2)\rangle + |2,2(B_1^1)\rangle,$$

which also has $d_{x^2-y^2}$ symmetry. When the effects of next-nearest neighbors are considered, the coefficients in the superposition of $|2,2(B_1^1)\rangle$ and $|2,2(B_1^2)\rangle$ are changed.

2. t - J_{\perp} - J_z Hamiltonian

Here we give the $|2\rangle$ and $|4\rangle$ ground states of the t - J_{\perp} - J_z Hamiltonian responsible for d -wave superfluidity (see Fig. 4). The s -wave symmetric $|1, 1\rangle$ ground state is

$$|1, 1(A_1)\rangle \propto a|1, 1(A_1^1)\rangle + |1, 1(A_1^2)\rangle \quad (C5)$$

with energy

$$E_g(1, 1) = -\frac{1}{16} \left[\sqrt{2048 - 2(4\sqrt{2} - 9) \left(\frac{J_{\perp}}{t} + 2 \frac{J_z}{t} \right)^2} + (4 + \sqrt{2}) \frac{J_{\perp}}{t} + 2(4 + \sqrt{2}) \frac{J_z}{t} \right],$$

where

$$a = \frac{1}{32\sqrt{2}} \left[\sqrt{2048 - 2(4\sqrt{2} - 9) \left(\frac{J_{\perp}}{t} + 2 \frac{J_z}{t} \right)^2} - (\sqrt{2} - 4) \frac{J_{\perp}}{t} - 2(\sqrt{2} - 4) \frac{J_z}{t} \right].$$

The d -wave symmetric $|2, 2\rangle$ ground state is

$$|2, 2(B_1)\rangle \propto b|2, 2(B_1^1)\rangle + |2, 2(B_1^2)\rangle \quad (C6)$$

with energy

$$E_g(2, 2) = \frac{1}{8} \left\{ - \left[130 \left(\frac{J_{\perp}}{t} \right)^2 + 16(2\sqrt{2} - 1) \frac{J_{\perp}}{t} \frac{J_z}{t} + 32(9 - 4\sqrt{2}) \left(\frac{J_z}{t} \right)^2 \right]^{1/2} + \sqrt{2} \frac{J_{\perp}}{t} - 16 \frac{J_z}{t} \right\},$$

where

$$b = \frac{1}{8} \frac{t}{J_{\perp}} \left\{ - \left[65 \left(\frac{J_{\perp}}{t} \right)^2 + 8(2\sqrt{2} - 1) \frac{J_{\perp}}{t} \frac{J_z}{t} + 16(9 - 4\sqrt{2}) \left(\frac{J_z}{t} \right)^2 \right]^{1/2} + \frac{J_{\perp}}{t} + (8\sqrt{2} - 4) \frac{J_z}{t} \right\}.$$

3. t - J - W Hamiltonian with $J_{\perp} = J_z = J$

Here we give the $|2\rangle$ and $|4\rangle$ ground states of the t - J - W Hamiltonian with $J_{\perp} = J_z = J$ responsible for d -wave superfluidity (see Figs. 5 and 6). Note that the following formulas do not depend on W in the sector where $|1, 1\rangle$ and $|2, 2\rangle$ are the ground states. The s -wave symmetric $|1, 1\rangle$ ground state is

$$|1, 1(A_1)\rangle \propto a|1, 1(A_1^1)\rangle + |1, 1(A_1^2)\rangle \quad (C7)$$

with energy

$$E_g(1, 1) = -\frac{1}{16} \left[\sqrt{18(9 - 4\sqrt{2}) \left(\frac{J}{t} \right)^2 + 2048} + 3(4 + \sqrt{2}) \frac{J}{t} \right], \quad (C8)$$

where

$$a = \frac{1}{32} \left[\sqrt{9(9 - 4\sqrt{2}) \left(\frac{J}{t} \right)^2 + 1024 + (6\sqrt{2} - 3) \frac{J}{t}} \right].$$

The d -wave symmetric $|2, 2\rangle$ ground state is

$$|2, 2(B_1)\rangle \propto b|2, 2(B_1^1)\rangle + |2, 2(B_1^2)\rangle \quad (C9)$$

with energy

$$E_g(2, 2) = \frac{1}{8} \frac{J}{t} \left[(\sqrt{2} - 16) - \sqrt{402 - 96\sqrt{2}} \right],$$

where

$$b = -\frac{\sqrt{201 - 48\sqrt{2}}}{8} \frac{J}{t} + \sqrt{2} - \frac{3}{8}.$$

We can understand the symmetries of the ground states of this Hamiltonian in the different sectors as follows. For large positive W , when the ground states are $|0, 2\rangle$ and $|0, 4\rangle$, the $|4\rangle$ Hilbert space is one dimensional with state

$$|0, 4(B_1)\rangle = |\downarrow\downarrow\downarrow\downarrow\rangle,$$

so the $|4\rangle$ state automatically has $d_{x^2-y^2}$ symmetry. In the limit of infinite W , the $|2\rangle$ ground subspace is a manifold consisting of two down spins next to each other. In this limit, the states in the A_2 and B_2 representations and the two states

$$\begin{aligned} |0, 2(E_x)\rangle &\propto |0\downarrow\downarrow 0\rangle + |\downarrow 00\downarrow\rangle + O\left(\frac{t}{W}\right) \\ |0, 2(E_y)\rangle &\propto |00\downarrow\downarrow\rangle + |\downarrow\downarrow 00\rangle + O\left(\frac{t}{W}\right) \end{aligned}$$

in the E representation are the ground states. For finite but large W , the $O(t/W)$ terms, proportional to $|0\downarrow 0\downarrow\rangle$ and $|\downarrow 0\downarrow 0\rangle$, make the p -wave symmetric states the ground states.

As W is decreased, the $|2\rangle$ ground state is s -wave $|1, 1\rangle$ since positive J_{\perp} and J_z make it favorable to have molecules of opposite spins. For intermediate values of J_{\perp} and J_z , the $|4\rangle$ ground state becomes $|1, 3\rangle$. With four molecules on a plaquette, there is no tunneling to consider in the energies of the states. Furthermore, since n_{\uparrow} and n_{\downarrow} are fixed, as determined by J_z , J_{\perp} , and W in this sector, we only have to consider the effects of J_{\perp} to explain the behavior of $|4\rangle$ in this sector. Consider two molecules of opposite spins on sites r and r' . The two eigenstates of the J_{\perp} interaction are $|\pm\rangle_{rr'}$ defined in Eq. (C4). Since $J_{\perp} > 0$, the singlet $|-\rangle_{rr'}$ is the ground state of the J_{\perp} interaction. Therefore, we may expect the $|1, 3\rangle$ ground state to be a superposition of singlets on nearest-neighbor bonds with relative phases chosen for constructive interference:

$$(s_{12}^{\dagger} t_{34}^{\dagger} + s_{23}^{\dagger} t_{41}^{\dagger} + s_{34}^{\dagger} t_{12}^{\dagger} + s_{41}^{\dagger} t_{23}^{\dagger}) |0\rangle.$$

Here

$$t_{rr'} = c_{r\downarrow}^{\dagger} c_{r'\downarrow}^{\dagger}$$

creates the $m = -1$ triplet state on sites r and r' , while $s_{rr'}$, defined in Eq. (4), creates the singlet state on sites r and r' . This state is indeed the $|1, 3\rangle$ ground state and has the s -wave A_2 symmetry.

- [1] P. A. Lee, N. Nagaosa, and X.-G. Wen, *Rev. Mod. Phys.* **78**, 17 (2006).
- [2] M. Ogata and H. Fukuyama, *Rep. Prog. Phys.* **71**, 036501 (2008).
- [3] E. Dagotto, *Rev. Mod. Phys.* **66**, 763 (1994).
- [4] U. Schneider, L. Hackermüller, S. Will, T. Best, I. Bloch, T. A. Costi, R. W. Helmes, D. Rasch, and A. Rosch, *Science* **322**, 1520 (2008).
- [5] R. Jördens, N. Strohmaier, K. Günter, H. Moritz, and T. Esslinger, *Nature (London)* **455**, 204 (2008).
- [6] J. Simon, W. S. Bakr, R. Ma, M. E. Tai, P. M. Preiss, and M. Greiner, *Nature (London)* **472**, 307 (2011).
- [7] J. F. Sherson, C. Weitenberg, M. Endres, M. Cheneau, I. Bloch, and S. Kuhr, *Nature (London)* **467**, 68 (2010).
- [8] I. Bloch, J. Dalibard, and W. Zwerger, *Rev. Mod. Phys.* **80**, 885 (2008).
- [9] S. Trotzky, P. Cheinet, S. Fölling, M. Feld, U. Schnorrberger, A. M. Rey, A. Polkovnikov, E. A. Demler, M. D. Lukin, and I. Bloch, *Science* **319**, 295 (2008).
- [10] S. Trotzky, Y.-A. Chen, U. Schnorrberger, P. Cheinet, and I. Bloch, *Phys. Rev. Lett.* **105**, 265303 (2010).
- [11] L. D. Carr, D. DeMille, R. V. Krems, and J. Ye, *New J. Phys.* **11**, 055049 (2009).
- [12] K.-K. Ni, S. Ospelkaus, M. H. G. de Miranda, A. Pe'er, B. Neyenhuis, J. J. Zirbel, S. Kotochigova, P. S. Julienne, D. S. Jin, and J. Ye, *Science* **322**, 231 (2008).
- [13] K. Aikawa, D. Akamatsu, M. Hayashi, K. Oasa, J. Kobayashi, P. Naidon, T. Kishimoto, M. Ueda, and S. Inouye, *Phys. Rev. Lett.* **105**, 203001 (2010).
- [14] J. Deiglmayr, A. Grochola, M. Repp, K. Mörtlbauer, C. Glück, J. Lange, O. Dulieu, R. Wester, and M. Weidemüller, *Phys. Rev. Lett.* **101**, 133004 (2008).
- [15] A. Chotia, B. Neyenhuis, S. A. Moses, B. Yan, J. P. Covey, M. Foss-Feig, A. M. Rey, D. S. Jin, and J. Ye, e-print [arXiv:1110.4420](https://arxiv.org/abs/1110.4420).
- [16] R. Barnett, D. Petrov, M. Lukin, and E. Demler, *Phys. Rev. Lett.* **96**, 190401 (2006).
- [17] A. Micheli, G. K. Brennen, and P. Zoller, *Nat. Phys.* **2**, 341 (2006).
- [18] G. K. Brennen, A. Micheli, and P. Zoller, *New J. Phys.* **9**, 138 (2007).
- [19] H. P. Büchler, A. Micheli, and P. Zoller, *Nat. Phys.* **3**, 726 (2007).
- [20] T. Watanabe, *Phys. Rev. A* **80**, 053621 (2009).
- [21] M. L. Wall and L. D. Carr, *New J. Phys.* **11**, 055027 (2009).
- [22] H. Yu, W. M. Liu, and C. Lee, e-print [arXiv:0910.4922](https://arxiv.org/abs/0910.4922).
- [23] R. V. Krems, W. C. Stwalley, and B. Friedrich, eds., *Cold Molecules: Theory, Experiment, Applications* (CRC Press, New York, 2009).
- [24] M. L. Wall and L. D. Carr, *Phys. Rev. A* **82**, 013611 (2010).
- [25] J. Schachenmayer, I. Lesanovsky, A. Micheli, and A. J. Daley, *New J. Phys.* **12**, 103044 (2010).
- [26] J. Pérez-Ríos, F. Herrera, and R. V. Krems, *New J. Phys.* **12**, 103007 (2010).
- [27] C. Trefzger, M. Alloing, C. Menotti, F. Dubin, and M. Lewenstein, *New J. Phys.* **12**, 093008 (2010).
- [28] F. Herrera, M. Litinskaya, and R. V. Krems, *Phys. Rev. A* **82**, 033428 (2010).
- [29] J. P. Kestner, B. Wang, J. D. Sau, and S. Das Sarma, *Phys. Rev. B* **83**, 174409 (2011).
- [30] A. V. Gorshkov, S. R. Manmana, G. Chen, E. Demler, M. D. Lukin, and A. M. Rey, *Phys. Rev. A* **84**, 033619 (2011).
- [31] A. V. Gorshkov, S. R. Manmana, G. Chen, J. Ye, E. Demler, M. D. Lukin, and A. M. Rey, *Phys. Rev. Lett.* **107**, 115301 (2011).
- [32] B. Liu and L. Yin, *Phys. Rev. A* **84**, 043630 (2011).
- [33] H. Yao, W.-F. Tsai, and S. A. Kivelson, *Phys. Rev. B* **76**, 161104 (2007).
- [34] W.-F. Tsai, H. Yao, A. Läuchli, and S. A. Kivelson, *Phys. Rev. B* **77**, 214502 (2008).
- [35] W.-F. Tsai and S. A. Kivelson, *Phys. Rev. B* **73**, 214510 (2006).
- [36] G. Karakonstantakis, E. Berg, S. R. White, and S. A. Kivelson, *Phys. Rev. B* **83**, 054508 (2011).
- [37] A. M. Rey, R. Sensarma, S. Fölling, M. Greiner, E. Demler, and M. D. Lukin, *Europhys. Lett.* **87**, 60001 (2009).
- [38] L. Isaev, G. Ortiz, and C. D. Batista, *Phys. Rev. Lett.* **105**, 187002 (2010).
- [39] S. Ospelkaus, K.-K. Ni, G. Quéméner, B. Neyenhuis, D. Wang, M. H. G. de Miranda, J. L. Bohn, J. Ye, and D. S. Jin, *Phys. Rev. Lett.* **104**, 030402 (2010).
- [40] Z. Idziaszek, G. Quéméner, J. L. Bohn, and P. S. Julienne, *Phys. Rev. A* **82**, 020703 (2010).
- [41] A. Micheli, Z. Idziaszek, G. Pupillo, M. A. Baranov, P. Zoller, and P. S. Julienne, *Phys. Rev. Lett.* **105**, 073202 (2010).
- [42] H. P. Büchler, E. Demler, M. Lukin, A. Micheli, N. Prokof'ev, G. Pupillo, and P. Zoller, *Phys. Rev. Lett.* **98**, 060404 (2007).
- [43] A. Micheli, G. Pupillo, H. P. Büchler, and P. Zoller, *Phys. Rev. A* **76**, 043604 (2007).
- [44] A. V. Gorshkov, P. Rabl, G. Pupillo, A. Micheli, P. Zoller, M. D. Lukin, and H. P. Büchler, *Phys. Rev. Lett.* **101**, 073201 (2008).
- [45] C.-H. Lin, Y.-T. Hsu, H. Lee, and D.-W. Wang, *Phys. Rev. A* **81**, 031601 (2010).
- [46] N. R. Cooper and G. V. Shlyapnikov, *Phys. Rev. Lett.* **103**, 155302 (2009).
- [47] M. Tinkham, *Group Theory and Quantum Mechanics* (Dover, Mineola, NY, 1964).
- [48] S. Trebst, U. Schollwöck, M. Troyer, and P. Zoller, *Phys. Rev. Lett.* **96**, 250402 (2006).
- [49] J. von Stecher, E. Demler, M. D. Lukin, and A. M. Rey, *New J. Phys.* **12**, 055009 (2010).
- [50] Y. Nagaoka, *Phys. Rev.* **147**, 392 (1966).
- [51] J. R. Schrieffer and P. A. Wolff, *Phys. Rev.* **149**, 491 (1966).
- [52] T. Giamarchi, *Quantum Physics in One Dimension* (Oxford University Press, Oxford, 2003).
- [53] F. Hébert, G. G. Batrouni, R. T. Scalettar, G. Schmid, M. Troyer, and A. Dorneich, *Phys. Rev. B* **65**, 014513 (2001).
- [54] G. G. Batrouni, R. T. Scalettar, G. T. Zimanyi, and A. P. Kampf, *Phys. Rev. Lett.* **74**, 2527 (1995).
- [55] R. T. Scalettar, G. G. Batrouni, A. P. Kampf, and G. T. Zimanyi, *Phys. Rev. B* **51**, 8467 (1995).
- [56] G. G. Batrouni and R. T. Scalettar, *Phys. Rev. Lett.* **84**, 1599 (2000).
- [57] E. Dagotto and J. Riera, *Phys. Rev. Lett.* **70**, 682 (1993).
- [58] E. Dagotto and J. Riera, *Phys. Rev. B* **46**, 12084 (1992).
- [59] K. Nelson, X. Li, and D. Weiss, *Nat. Phys.* **3**, 556 (2007).
- [60] S. Peil, J. V. Porto, B. Laburthe Tolra, J. M. Obrecht, B. E. King, M. Subbotin, S. L. Rolston, and W. D. Phillips, *Phys. Rev. A* **67**, 051603 (2003).

- [61] J. E. Curtis, B. A. Koss, and D. G. Grier, *Opt. Commun.* **207**, 169 (2002).
- [62] A. S. Sørensen, E. Altman, M. Gullans, J. V. Porto, M. D. Lukin, and E. Demler, *Phys. Rev. A* **81**, 061603 (2010).
- [63] L.-M. Duan, E. Demler, and M. D. Lukin, *Phys. Rev. Lett.* **91**, 090402 (2003).
- [64] S. Kotochigova and D. DeMille, *Phys. Rev. A* **82**, 063421 (2010).
- [65] E. Altman, E. Demler, and M. D. Lukin, *Phys. Rev. A* **70**, 013603 (2004).
- [66] I. B. Spielman, W. D. Phillips, and J. V. Porto, *Phys. Rev. Lett.* **98**, 080404 (2007).
- [67] M. Lu, N. Q. Burdick, S. H. Youn, and B. L. Lev, *Phys. Rev. Lett.* **107**, 190401 (2011).
- [68] A. Griesmaier, J. Werner, S. Hensler, J. Stuhler, and T. Pfau, *Phys. Rev. Lett.* **94**, 160401 (2005).
- [69] R. Schumann, *Ann. Phys. (NY)* **11**, 49 (2002).
- [70] G. Fano, F. Ortolani, and A. Parola, *Phys. Rev. B* **46**, 1048 (1992).